Chapter 7

On-Body Flow Visualisation

The flow field associated with patterns of skin friction lines (also called surface streamlines) has been the subject of extensive investigation and review [63][64][11]. These investigations are generally based on the concept that streamlines adjacent to the surface may be described by a vector field, except at singular points. The nature of these singularities is critical to the description of the flow; they may be broadly categorised as nodes or saddles, with foci and centres being subsets of nodes. The topology of these singularities is shown in Appendix E.

Working with spheroids at high incidence (40°), Wang [65] numerically demonstrated the existence of open separations (or cross-flow separations). These are separation lines where skin friction lines emanating from a single node of attachment converge on a separation line from both sides. The existence of open separations ran contrary to the accepted models of the time, requiring separation lines to emanate from a saddle point (closed separation). The figure from Wang [65] showing the two types of flow separation is reproduced in Fig. 7.1. Cebeci et al. [40] further examined open separations numerically. As a singularity in the vector field is not required for the start or finish of an open separation, Simpson [66] suggested

> "a definition of the upstream beginning of an open separation line is where multiple skin-friction lines first converge to a single line"

while Wu et al. [67] provided a "working definition" for open and closed separations as follows:

> "A flow separates from a wall if and only if a free shear layer is formed adjacent to the wall and leaves it."

The convergence of surface streamlines at an open separation is not associated with a boundary layer separation, but if flow from either side of the separation line has different velocities it will create a free shear layer as the converging flow leaves the surface. Wu et al. [67] provide a discussion of boundary layer versus flow separation.

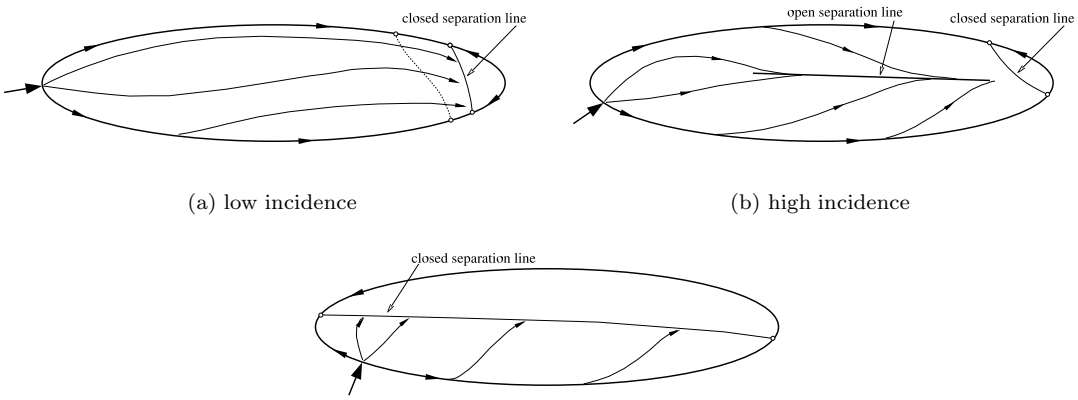

(a) low incidence

(b) high incidence

(c) extremely high incidence

Figure 7.1: Arrows indicate the limiting streamlines. (see Wang [65] Figure 1)

Unfortunately as off-body visualisation and measurements are not available in the relevant region, the latter of these definitions does not assist the interpretation of surface flow visualisation. The first definition may be misused if applied to skin friction lines approaching a node of separation (e.g. Fig. 7.17). Simpson's definition is used in the present study, as it allows the classification of open separations from surface flow visualisation.

Han and Patel [15] visually examined the flow around a 4.3–1 spheroid using dye and surface-mounted wool tufts at a relatively low Reynolds numbers ($Re_l = 0.25 \times 10^6$ to 0.7×10^6) and detailed the role of azimuthal pressure gradients in the development of open type separations. Meier et al. [20] calculated surface streamlines from wall shear stress measurements on their 6–1 spheroid. Both these papers report the existence of an open separation at $\alpha = -10°$ when the flow approaching this separation is laminar (Meier et al. $Re_l = 1.6 \times 10^6$). In the same paper, Meier et al. report the presence of an open separation when the flow approaching the separation is turbulent at $\alpha = -10°$ for the same model ($Re_l = 7.2 \times 10^6$).

7.1 Test Setup

The spheroid and ellipsoid model with grid, along with the previously detailed support foil and stings, were used in this testing. The on-body flow visualisation was performed using a mixture of oil and titanium white (titanium dioxide). Wetzel et al. [30] report

- gravity effects, and
- interactions between flow fields and oil

as shortcomings of using oil-flow visualisation to detect separation and its location. The use of water as the working fluid allows the selection of a neutrally buoyant (or nearly so) oil to negate the influence of gravity. Using a selection of different viscosity oils that result in a different thickness of oil allows interactions between the flow field and oil to be observed. Squire's [68] numerical studies conclude that oil-flow visualisation result in a premature indication of separation which is independent of viscosity but dependent on oil film thickness. In practice the use of different viscosity oils will lead to different oil film thickness. Squire [68] states, "Thus, in general, the oil will only have a small influence on the boundary layer, changing the distance to separation by at most 2%.". Repeating the test with different viscosity mixtures incurs a significant time penalty in a cavitation tunnel as it requires the water to be lowered, the top window unbolted, the model cleaned, oil reapplied, top window rebolted, and the tunnel refilled. Testing with different viscosity oils at the same Reynolds number is, however, useful when performed judiciously. Oils based on hydrocarbons must be avoided, as they may damage the acrylic test section windows. Fortunately the Dow Corning® 200 fluid, selected for use inside the housing of the force/torque transducer, has the desirable properties listed above: it has a specific density of approximately 0.95 and is available in a large range of viscosities. The chemical name of this fluid is Polydimethylsiloxane. A $10:1$ ratio by weight of Dow Corning® 200 fluid to titanium white was used. Titanium white has a specific density of 3.77. The Dow Corning® 200 fluid is available in a range of viscosities from $0.65\,cSt$ to $60000\,cSt$. A range from $10\,cSt$ to $5000\,cSt$ was used in the present study; this is approximately 11 to 5500 times the kinematic viscosity of water at $25°C$. The estimated density of a subset of the mixtures used in this flow visualisation is given in Table 7.1. The viscosity of the mixture will vary from that of the fluid; however this was not measured. The mixtures created from the lower viscosity fluids were used at lower Reynolds numbers. At the lowest Reynolds numbers flow visualisation was tested, $Re_l = 1.0 \times 10^6$, only limited success was achieved with this technique or similar methods using a higher ratio of Dow Corning® 200 fluid to titanium white.

Optical access to the test section is available through $110\,mm$ thick acrylic side windows or via $85\,mm$ thick acrylic windows on the bottom. To minimise distortion due to refraction when taking photos at non-normal angles, small viewing windows were designed and manufactured. These are essentially open-topped boxes with angled sides and a flange around the opening. A gasket or o-ring on the flange sealed the opening against the side window of the tunnel; two horizontal bars held the viewing window in place. Once sealed against the side window the viewing window was filled with water. The compound viewing window shown in Fig. 7.2 is angled for viewing the model from above/behind or below/ahead of the model. Manufacture of a simple 30° window allowed viewing from straight ahead or behind. Two Canon 300D

Dow Corning® 200 fluid	kinematic viscosity (m^2/s)	absolute viscosity $(Pa.s)$	specific density of fluid (kg/m^3)	specific density of mixture (kg/m^3)
$10\,cSt$	10×10^{-6}	9.34×10^{-3}	0.934	1.00
$100\,cSt$	100×10^{-6}	9.60×10^{-2}	0.960	0.97
$1000\,cSt$	1000×10^{-6}	0.971	0.971	0.96
$5000\,cSt$	5000×10^{-6}	4.88	0.975	0.96

Table 7.1: Properties of Dow Corning® 200 fluid at $25°C$ and density of mixture with titanium white.

digital cameras were mounted to the tunnel via adjustable stands. These recorded the flow visualisation at the rear of the model: one from above, and the other from below, focussed through the compound windows. A sequence of photos were taken so the visualisation pattern could be observed over time, this ensured that a stable pattern had been achieved and allowed greater insight as the convection of the oil mixture may be examined. Lighting was provided from the side and below the model. The overall setup is shown in Fig. 7.3. Fig. 7.4 shows the lens of the camera in position approximately parallel to the panel of the viewing window.

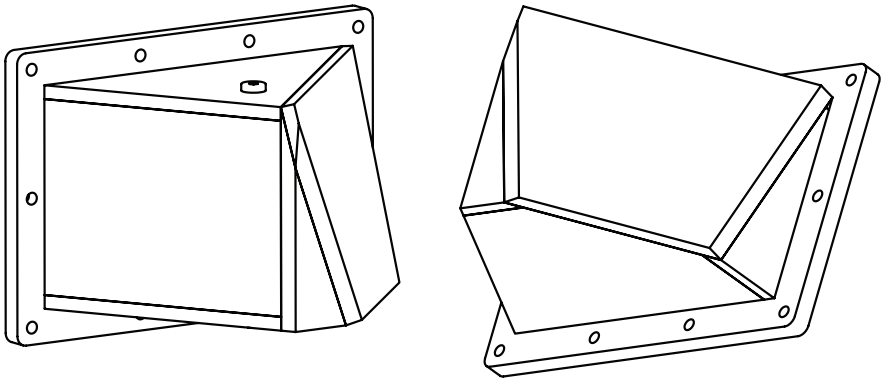

Figure 7.2: Compound viewing window used to reduce refraction

Flow visualisation around the front of the model was performed for the ellipsoid model for a limited number of cases. This required additional tests due to limited cameras and lighting. Surface streamlines have been drawn overlaying the photos for many of the cases. These surface streamlines have been traced from full resolution photos.

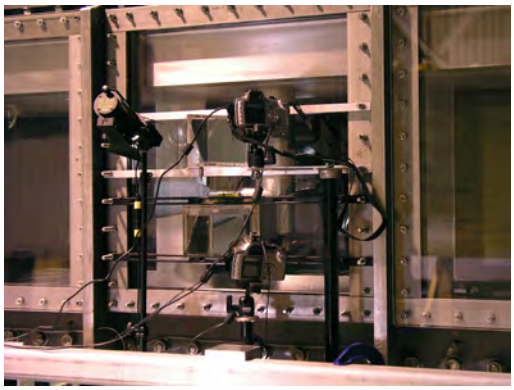

Figure 7.3: Camera and light setup for flow visualisation

Figure 7.4: Closeup of cameras and viewing windows

7.2 3–1 Spheroid Flow Visualisation

Over the front of the model, where in most cases no visualisation was performed, streamlines are drawn from the classical potential flow solution. These streamlines (not surface streamlines) should provide a reasonable guide to the bulk flow direction outside the boundary layer around the front of the model, where the displacement thickness is small.

The nodes, foci, and saddles are marked on the figures with the letters N, F, and S respectively. When the existence of a node or saddle is not directly apparent from the visualisation, but is deduced from symmetry or some other reasoning, the letter will be coloured cyan. A case in point is the node at the base. When the flow separates from the body just prior to the sting the recirculation of the flow will result in a short length of flow in the upstream direction along the sting. This flow results in an effective node of attachment where the sting and ellipsoid meet in the region of separated flow. This node is not visible, as no oil is placed on the sting and a small gap exists between the sting and model.

Han and Patel [15] positioned their model using eight wires, thus reducing the interference at the rear. The results from their test at low ($\alpha = 5°$) and moderate ($\alpha = 10°$) angles of incidence show a node of attachment in the region of separated flow at the rear of the model. This node is shown in cyan on the figures in this paper; other singularities that are inferred will be discussed as relevant. A node of attachment is shown at the nose of the model as determined from the potential calculations.

Examination of surface streamlines produced from CFD reveal the existence of nodes and saddles that have relatively small localised influence. In regions of separated flow little, if any, oil mixture may reach these singularities. Thus some singularities are difficult to detect using oil-flow visualisation.

Where a mesh is added to the photos it is manually aligned to the grid over the primary

area of interest. Due to distortion in the photograph the alignment between the grid and photo deteriorates away from the focal point. Surface streamlines at the rear of the model have been sketched on the grid using full resolution upper and lower views, and are shown in dark blue. Streamlines determined from classical potential calculations over the front of the model are shown in light green, and are referred to in the text as potential streamlines.

7.2.1 Spheroid at $\alpha = -10.2°$, Boundary Layer Tripped at 20% of Total Length

The higher angle of incidence is examined initially as the greater azimuthal pressure gradients and the turbulent boundary layer results in well-defined visualisation. The following discussion focuses on the results for $Re_l = 4.0 \times 10^6$; the results at 2.0×10^6 and 3.0×10^6 are similar.

Fig. 7.5 shows a large separated region on the flank of the model. A focus of separation is apparent at $x_{bc}/l \approx 0.48$, $\varphi \approx -30°$ and a node of separation at $x_{bc}/l \approx 0.44$, $\varphi \approx -150°$. A saddle exists at $x_{bc}/l \approx 0.38$, $\varphi \approx -130°$, but is better seen in Fig. 7.6 where a slightly thicker coat of oil has improved visualisation of the flow in the separated region (the strobe used to illuminate the under side of the model has failed to trigger). Assuming the same topology exists on the other side of the symmetry plane a total of four nodes (nose, sting and two in the separated region), two foci and four saddles exist. This topology is consistent with the requirement that the number of nodes (including foci) should exceed the number of saddles by two [69]. The saddle on the side ($x_{bc}/l \approx 0.38$, $\varphi \approx -130°$) is, however, at odds with the description of Han and Patel [15] that designates a singularity at a similar physical and topological location as a node in their description of the surface streamlines at low and moderate incidence.

There appears to be reasonable alignment between the potential streamlines and those drawn from the photo where they meet near the centre of the model. This observation implies that in this case there is minimal azimuthal pressure gradient where they meet. The existence of saddle points on the pressure and suction sides of the plane of symmetry near the base is expected, as the flow separates on the symmetry plane upstream of the sting. The saddle point occurs on the symmetry plane at the junction between the fluid moving upstream along the surface in the separated region and flow moving downstream where it is still attached. Fig. 7.7 shows the saddle point on the suction side of the symmetry plane.

The flank separation towards the rear of the model is a result of the adverse pressure gradient in the azimuthal and longitudinal direction and the prior thickening of the boundary layer. On initial consideration, a region of separated flow on the suction side of the symmetry plane near the sting may be expected. However, separation on the flank occurs upstream of

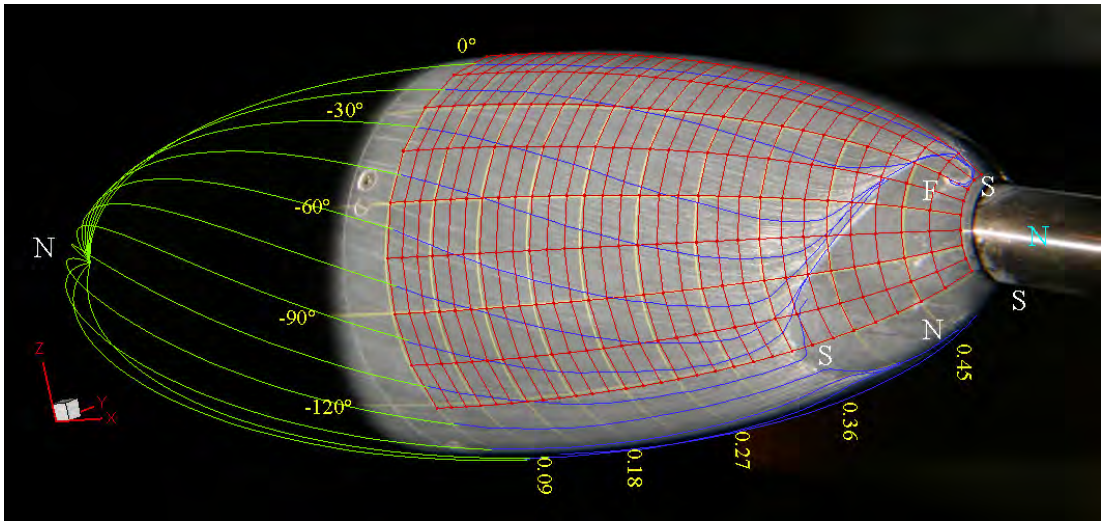

(a) Upper View

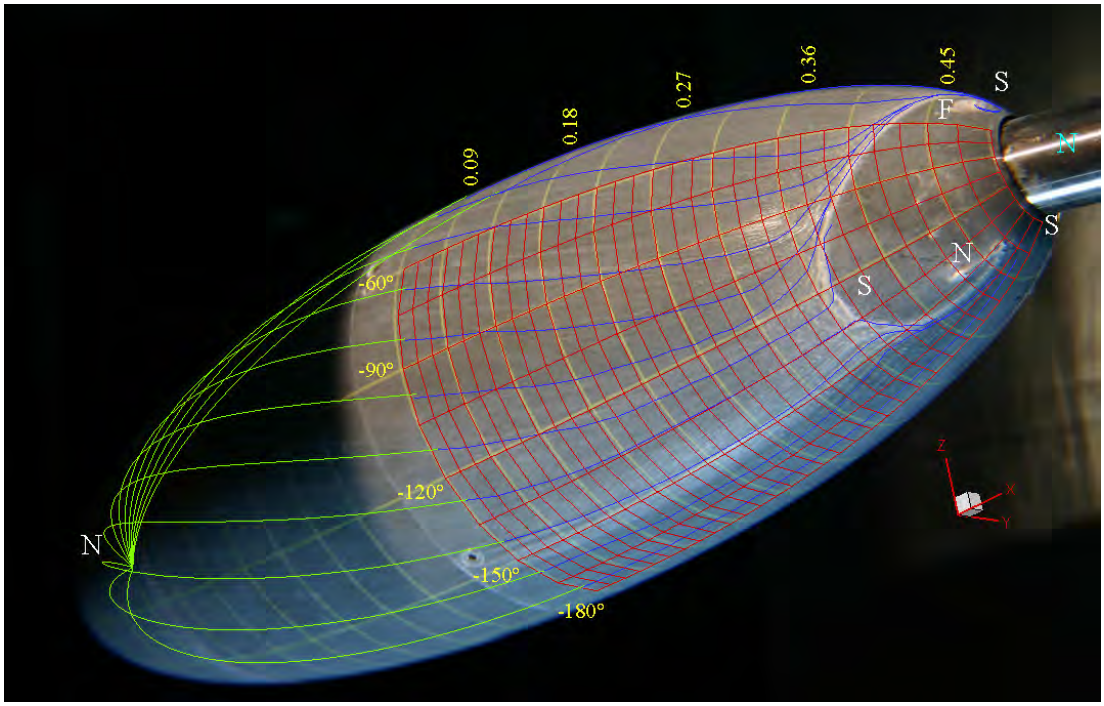

(b) Lower View

Figure 7.5: Surface flow visualisation on spheroid, $\alpha = -10.2°$, boundary layer tripped at $x_{bc}/l = -0.3$, $Re_l = 4.0 \times 10^6$. A large separated region dominates the rear of the model. Near the symmetry plane on the pressure side the flow separates shortly before the sting.(Axes aligned with body coordinates, streamwise grids marked with x_{bc}/l values, green surface streamlines calculated from classical potential theory, blue surface streamlines drawn from underlying photo.)

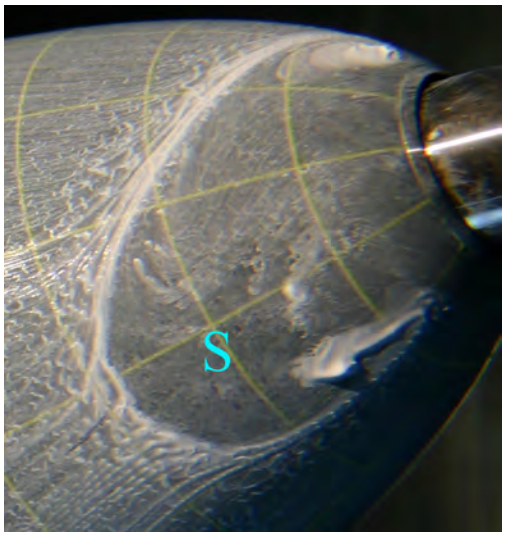

Figure 7.6: Oil within separated region displaying existence of flank saddle, $\alpha = -10.2°$, $Re_l = 4.0 \times 10^6$

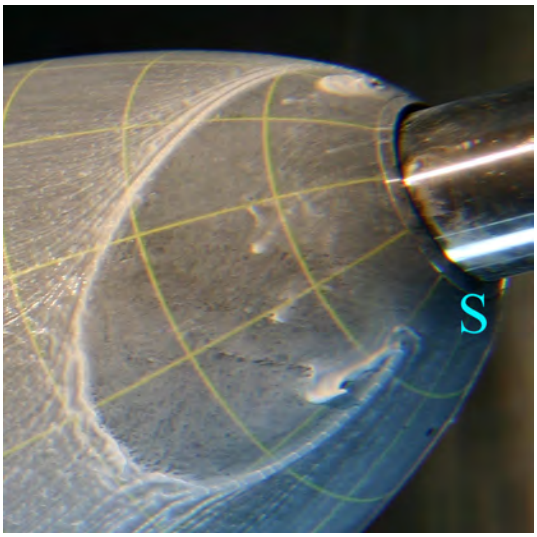

Figure 7.7: Close up of lower saddle, $\alpha = -10.2°$, $Re_l = 4.0 \times 10^6$

the region where the flow encounters a strong adverse pressure gradient on the suction side of the symmetry plane. Fig. 7.8 shows the potential streamlines and non-dimensional pressure gradient calculated from the classical potential solution. The separation on the flank of the model prevents the surface streamlines from converging on the suction side of the symmetry plane. A narrow tongue of flow stays attached to within half a grid spacing ($x_{bc} \approx 0.024$) of the end of the model on the suction side of the symmetry plane. The argument that a separation on the flank of the model prevents the surface streamlines converging on the suction side of the symmetry plane is used by Han and Patel in their description of the influence of open separations, the open separations in their description occur well upstream of the closed separation that exists in this case. The slight gradient in the surface pressure curves on the symmetry plane noted in Subsection 4.4.4 does not provide definitive evidence as to the state of attachment of the boundary layer. Thus the attachment of a narrow tongue of fluid between the separations on either side of the symmetry plane is not inconsistent with the results from the surface pressure measurements.

7.2.2 Spheroid at $\alpha = -10.2°$

$Re_l = 2.0 \times 10^6$

Boundary layer transition was not generally observed in the flow visualisation results. Fig. 7.9(a) is one of the few cases where the region of boundary layer transition may be determined from the flow visualisation; it is indicated by the cyan line on the surface for φ between 0° and

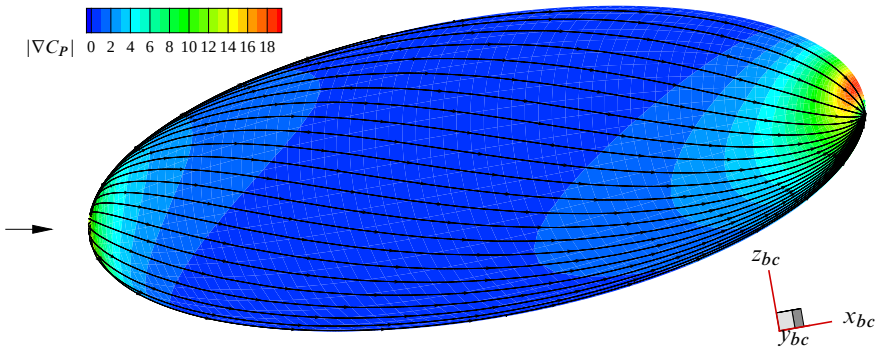

Figure 7.8: Potential streamlines and non-dimensional pressure gradient magnitude for spheroid at $\alpha = -10.2°$. Potential theory shows the surface streamlines converging on the suction side of the symmetry plane. (Model rotated 30° about z-axis, Non-dimensionalisation by freestream dynamic pressure and model length)

$-90°$. Here transition to turbulence is indicated by greater scouring of the oil mixture on the surface associated with the higher wall shear stress in turbulent flow regions. The black line on Fig. 7.9 indicates the boundary layer transition position estimated from the surface pressure measurements.

There is a deviation in the surface streamlines near $x_{bc} = 0.27$, $\varphi = -75°$ and $x_{bc} = 0.22$, $\varphi = -88°$. The potential streamlines over the front of the body and those drawn from flow visualisation appear to align for φ between 0° and $-100°$. There exists a clear discontinuity between calculated and drawn lines on the suction side for φ between $-100°$ and $-150°$. The streamlines between $-100°$ and $-150°$ appear to have been diverted from converging on the suction side of the symmetry plane. This may be explained if the observed deviation is due to the flow being deflected by an increased resistance associated with the turbulent boundary layer. This deflection is apparent when the flow is at a glancing angle to the transition line.

The topology of the singularities seen in Fig. 7.9 is similar to that described for the spheroid when the trip strip is employed. It differs in that the focus associated with the separation on the flank of the model is now designated as a node. The separation on the flank of the model is smaller and has shifted on the suction side so it is centred at $\varphi = -150°$. Another photo (Fig. 7.10) of the upper surface under the same condition using a less viscous oil mixture reveals that a short ($5\,mm$) laminar separation bubble exists between $\varphi = 0°$ and $\varphi = -50°$ in the region where boundary layer transition ($x_{bc} \approx 0.41$) is located. This separation bubble is too short to be detected by the pressure taps, due to their relatively coarse placement. Fig. 7.10 shows the same streamlines as Fig. 7.9 with the underlying mesh turned off to allow better viewing of the laminar separation bubble. This separation bubble appears almost two-dimensional, with no apparent flow along the separation line or deviation of the surface streamlines in the azimuthal direction leading to or from the separation bubble.

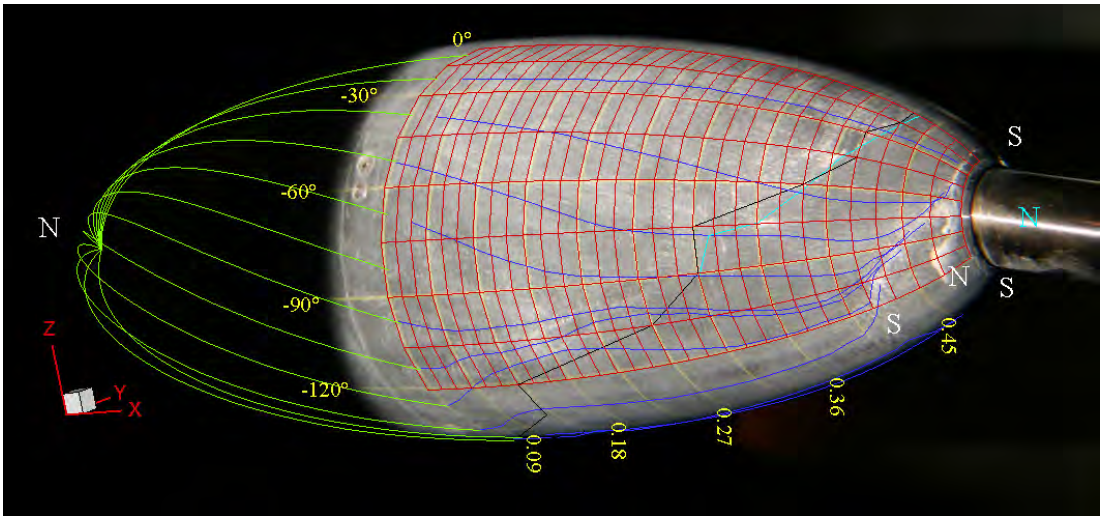

(a) Upper View. Boundary layer transition estimated from the flow visualisation is indicated by the cyan line for φ between $0°$ and $-90°$.

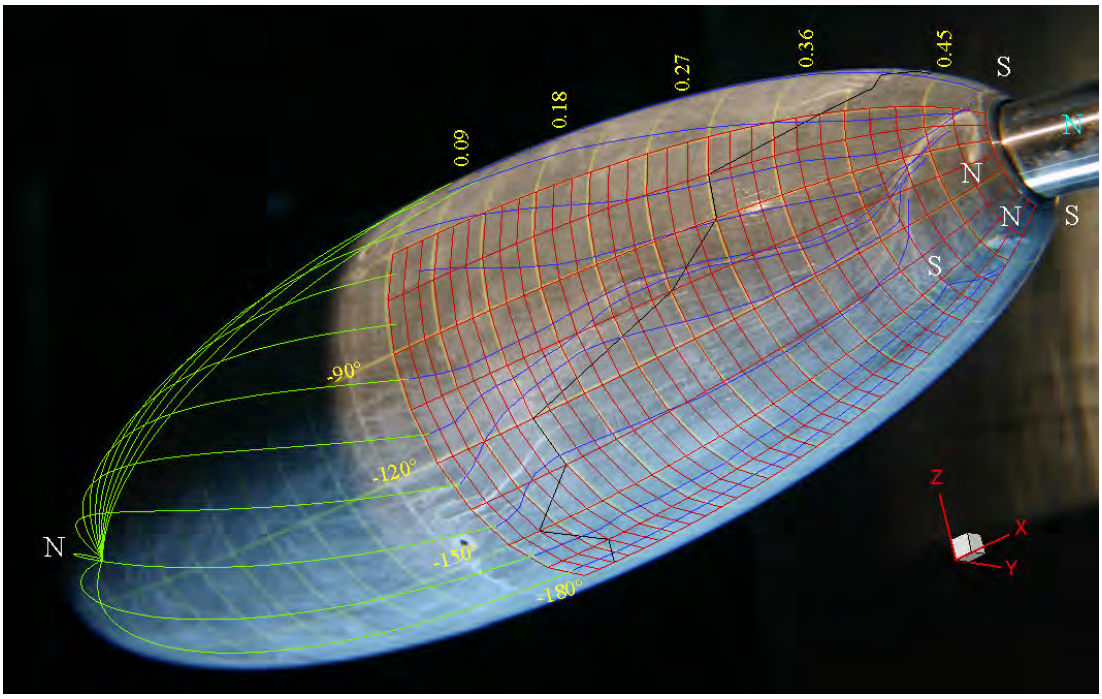

(b) Lower View, perturbations in the streamlines determined from the flow visualisation appear to coincide with the location of transition estimated from the surface pressure.

Figure 7.9: Surface flow visualisation on spheroid, $\alpha = -10.2°$, $Re_l = 2.0 \times 10^6$. The black line shows the estimated location of boundary layer transition determined from the measured surface C_p distribution. (Axes aligned with body coordinates, streamwise grids marked with x_{bc}/l values, green surface streamlines calculated from classical potential theory, blue surface streamlines drawn from underlying photo.)

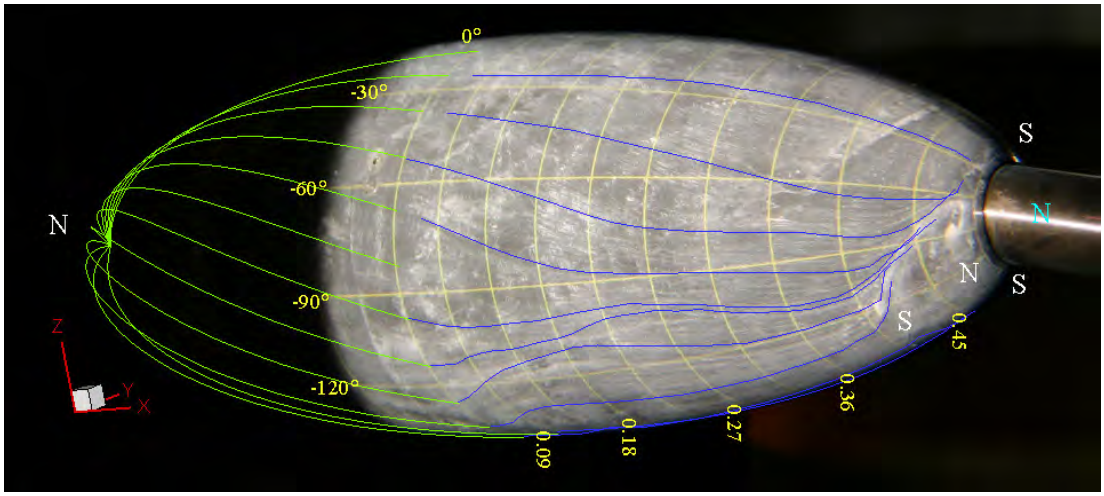

Figure 7.10: Laminar separation bubble at $x_{bc}/l \approx 0.41$ for φ between 0° and $\varphi = -50°$. This bubble only became apparent with the use of a lower viscosity oil mixture. Spheroid at $\alpha = -10.2°$, $Re_l = 2.0 \times 10^6$. (Axes aligned with body coordinates, streamwise grids marked with x_{bc}/l values, green surface streamlines calculated from classical potential theory, blue surface streamlines drawn from underlying photo.)

$Re_l = 4.0 \times 10^6$

Fig. 7.11 shows that the singularities and surface streamlines at $Re_l = 4.0 \times 10^6$ are very similar to those of the spheroid when the trip strip was employed (Section 7.2.1). The minor difference is that:

- the singularity near $x_{bc}/l \approx 0.44$, $\varphi = -120°$ is now a focus
- the focus towards the pressure side of this separation appears to be less dominant ($x_{bc}/l \approx 0.47$, $\varphi = -60°$)
- the flow on the pressure side of the symmetry plane stays attached later, until the metal ring at the end of the model
- the width of the attached flow on the pressure side of the symmetry plane flow extends out from the symmetry plane in the azimuthal direction by 30° instead of less than 10°.

In contrast to the results of Meier et al. [20] and Han and Patel [15], no convergence of the surface streamlines on the flank of this lower aspect ratio spheroid is observed in Figs. 7.5, 7.9 or 7.11.

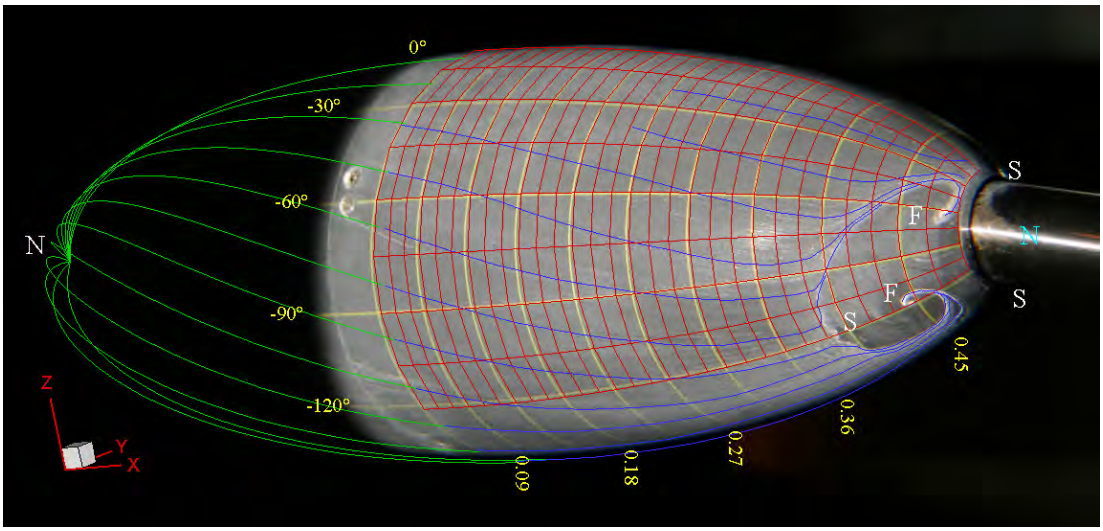

(a) Upper View

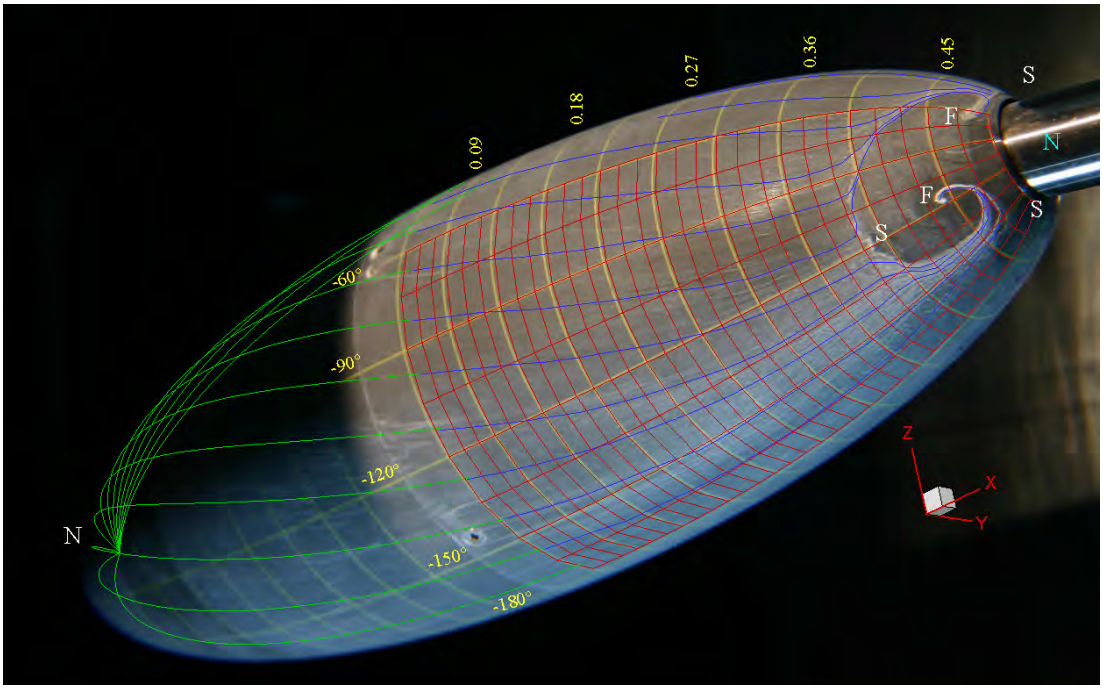

(b) Lower View

Figure 7.11: Surface flow visualisation on spheroid, $\alpha = -10.2°$, $Re_l = 4.0 \times 10^6$. The flow visualisation is similar to that seen at this incidence and Reynolds number when boundary layer was tripped at $x_{bc}/l = -0.3$. (Axes aligned with body coordinates, streamwise grids marked with x_{bc}/l values, green surface streamlines calculated from classical potential theory, blue surface streamlines drawn from underlying photo.)

7.2.3 Spheroid at $\alpha = -6.2°$

$Re_l = 2.0 \times 10^6$

The surface streamline pattern for this flow is not dominated by large obvious singularities associated with the region of separation. The separation at the rear of the model stays attached marginally longer on the pressure side and has numerous small saddles and nodes (Fig. 7.12). This node-saddle combination is associated with two dimensional separations [11].

Near the centre of the body, where potential streamlines and those drawn from the surface visualisation meet, the curves are aligned for φ between 0° and −100°. For φ between −100° and −150° the surface streamlines are deflected towards the pressure side. This deflection appears similar, though smaller than, that seen at this Reynolds number in Subsection 7.2.2. It occurs a small distance upstream of the estimated transition line when the surface streamline and transition lines meet at a relatively small angle.

$Re_l = 3.8 \times 10^6$

The singularities apparent at $\alpha = -6.2°$, $Re_l = 3.8 \times 10^6$ are the same as seen for $\alpha = -10.2°$, $Re_l = 4.0 \times 10^6$. In other comparisons between these two cases:

- the size of the separation is smaller and its centre further towards the pressure side of the model, $\varphi \approx -85°$
- the flow near the pressure and suction sides of the symmetry plane appears to be separating at a similar location.

There is a small asymmetry in the flow visualisation across the symmetry plane on the suction side. The potential and drawn surface streamlines are aligned where they meet near $x_{bc}/l \approx 0.14$.

7.2.4 Spheroid at $\alpha = -0.2°$

$Re_l = 2.0 \times 10^6$

The surface streamlines are aligned with the grid lines on the model for $Re_l = 2.0 \times 10^6$ in Fig. 7.14 until $x_{bc}/l \approx 0.45$, except near $\varphi = -180°$ where the alignment exists until $x_{bc}/l \approx 0.41$. Ideally the flow separation will be axisymmetric. However in the absence of significant azimuthal pressure gradients minor factors may play a significant role in the flow. This will be exacerbated by the highly sensitive nature of separation from a curved surface.

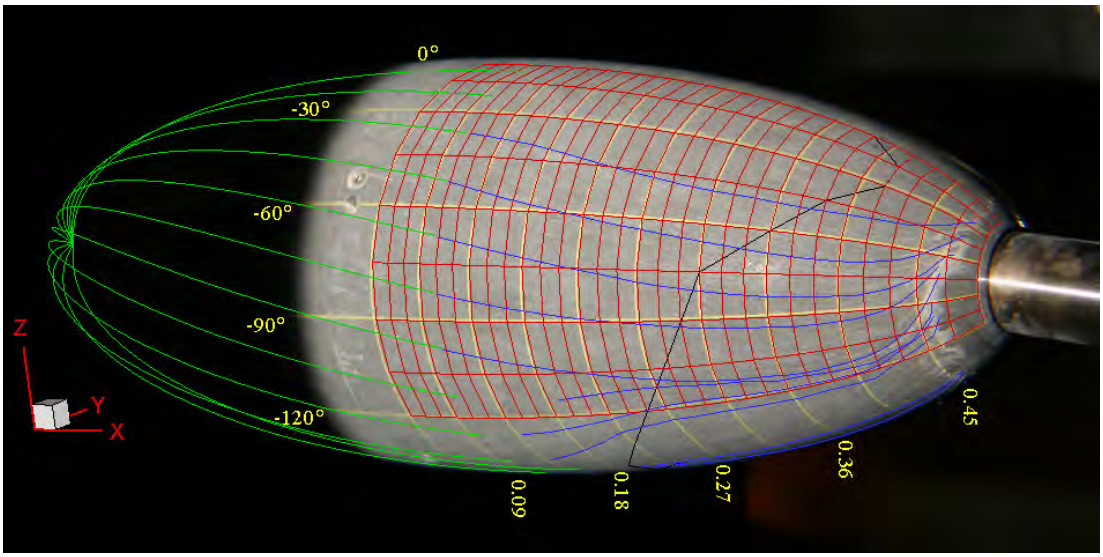

(a) Upper View

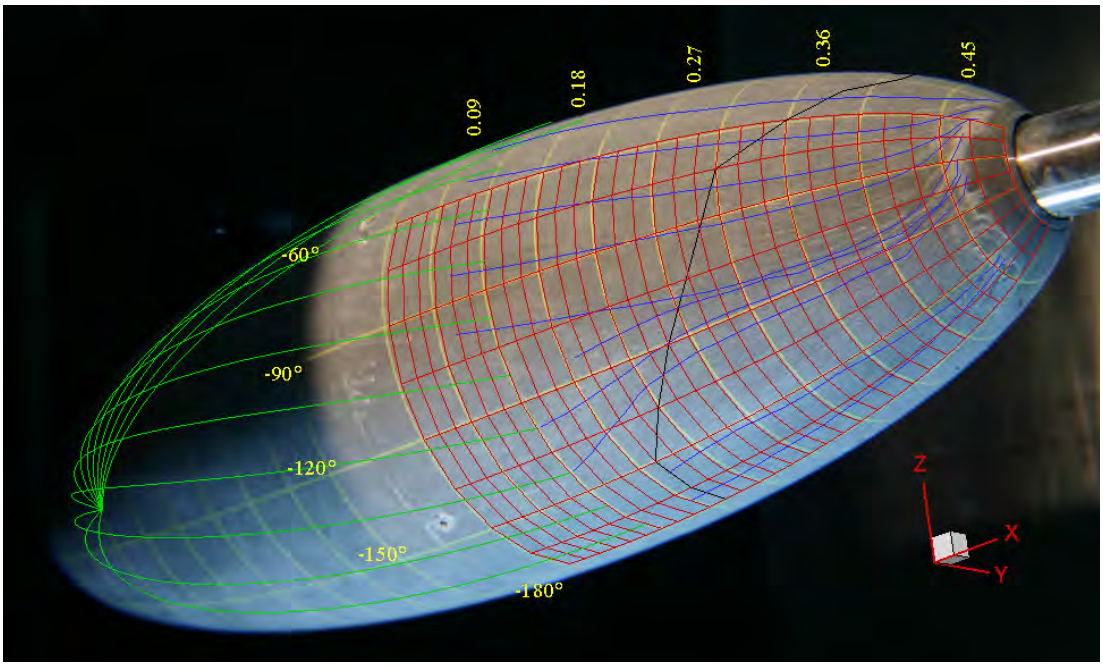

(b) Lower View (Potential streamlines extended by $x_{bc}/l \approx 0.05$)

Figure 7.12: Surface flow visualisation on spheroid, $\alpha = -6.2°$, $Re_l = 2.0 \times 10^6$. The black line shows the estimated location of boundary layer transition determined from the measured surface C_p distribution. Boundary layer separation is characterised by small nodes and saddles. (Axes aligned with body coordinates, streamwise grids marked with x_{bc}/l values, green surface streamlines calculated from classical potential theory, blue surface streamlines drawn from underlying photo.)

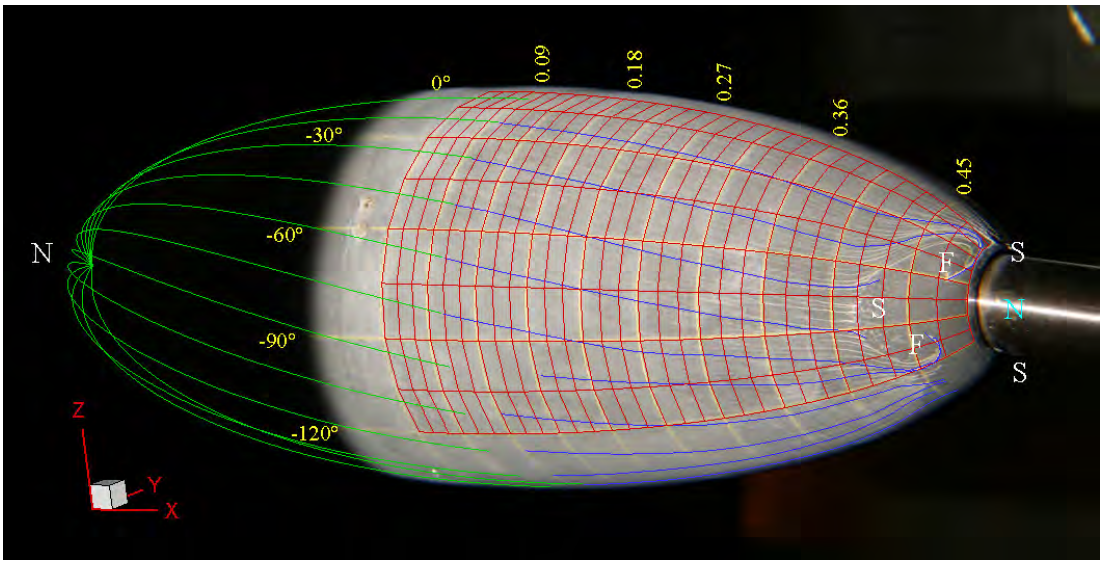

(a) Upper View

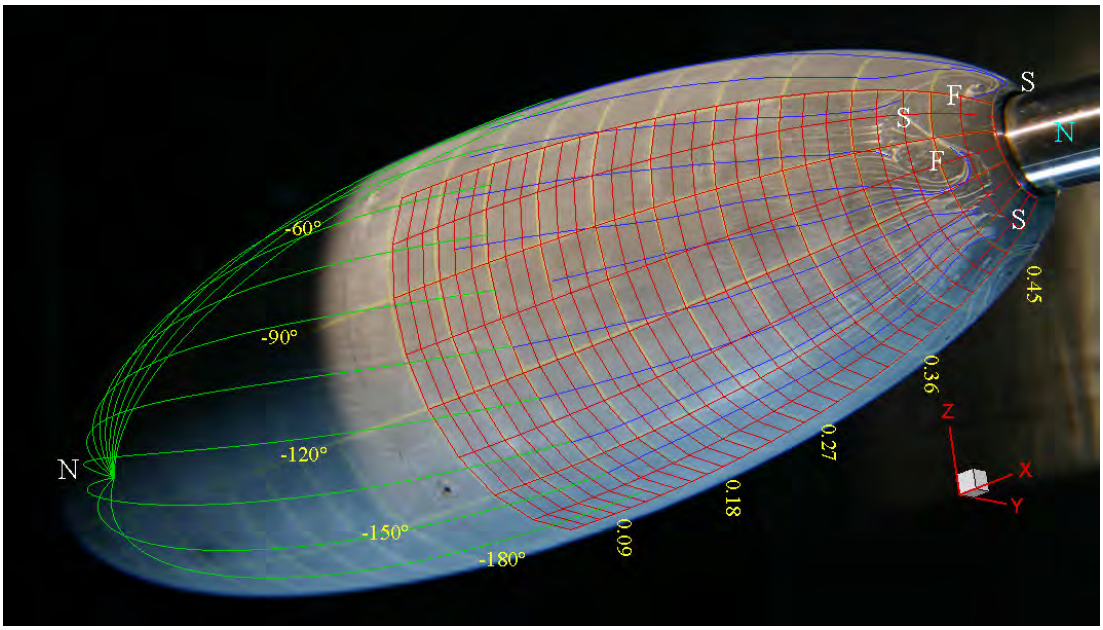

(b) Lower View (Potential streamlines extended by $x_{bc}/l \approx 0.05$)

Figure 7.13: Surface flow visualisation on spheroid, $\alpha = -6.2°$, $Re_l = 3.8 \times 10^6$. Similar surface singularities as seen at $\alpha = -10.2°$, $Re_l = 4.0 \times 10^6$ with a smaller separation on the flank. (Axes aligned with body coordinates, streamwise grids marked with x_{bc}/l values, green surface streamlines calculated from classical potential theory, blue surface streamlines drawn from underlying photo.)

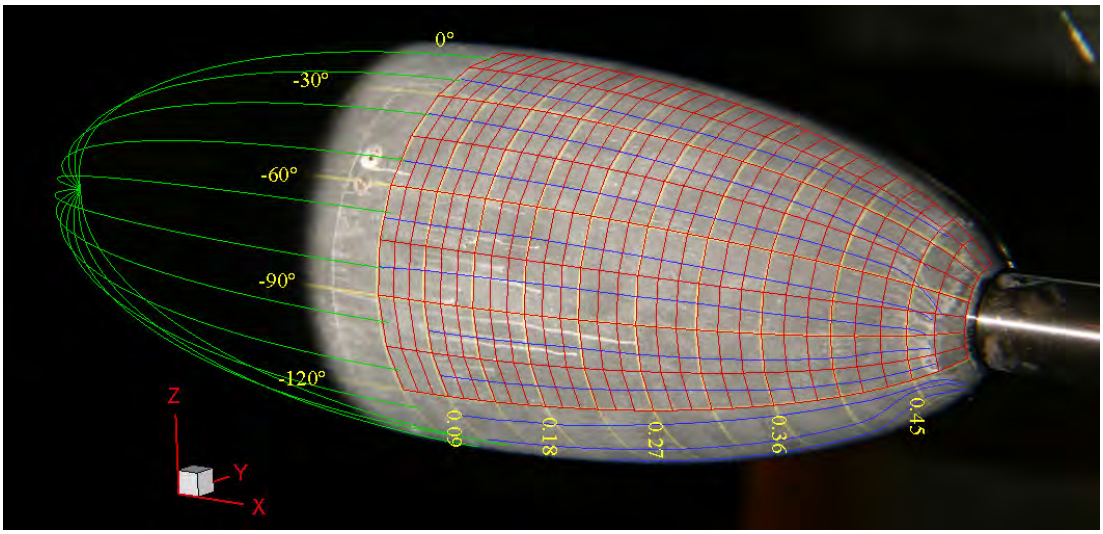

(a) Upper View

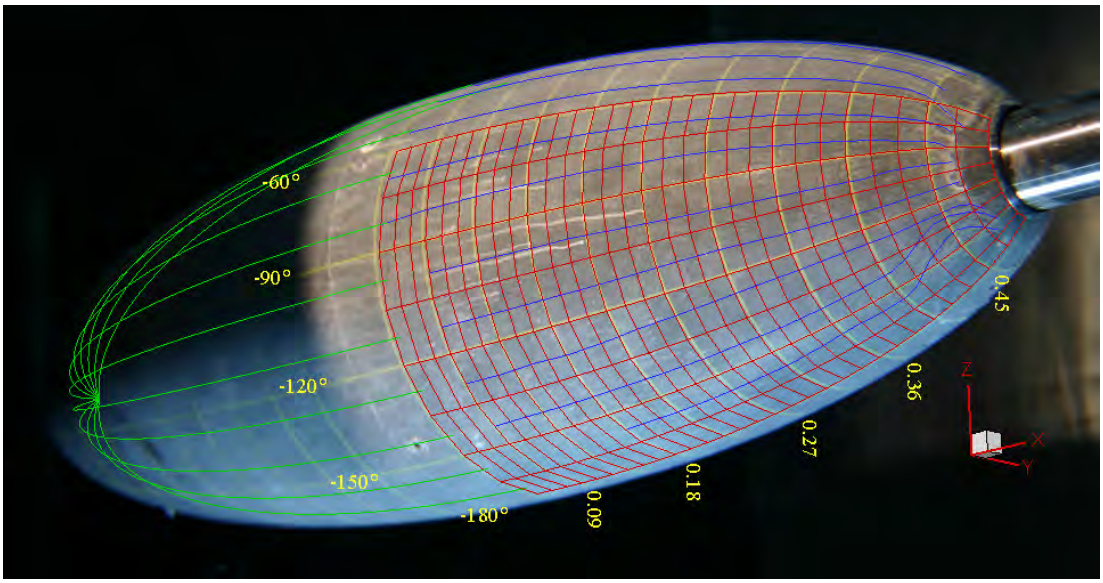

(b) Lower View

Figure 7.14: Surface flow visualisation on spheroid, $\alpha = -0.2°$, $Re_l = 2.0 \times 10^6$. The surface streamlines appear axisymmetric until the last 5% to 10% of the body when minor perturbations are apparent.(Axes aligned with body coordinates, streamwise grids marked with x_{bc}/l values, green surface streamlines calculated from classical potential theory, blue surface streamlines drawn from underlying photo.)

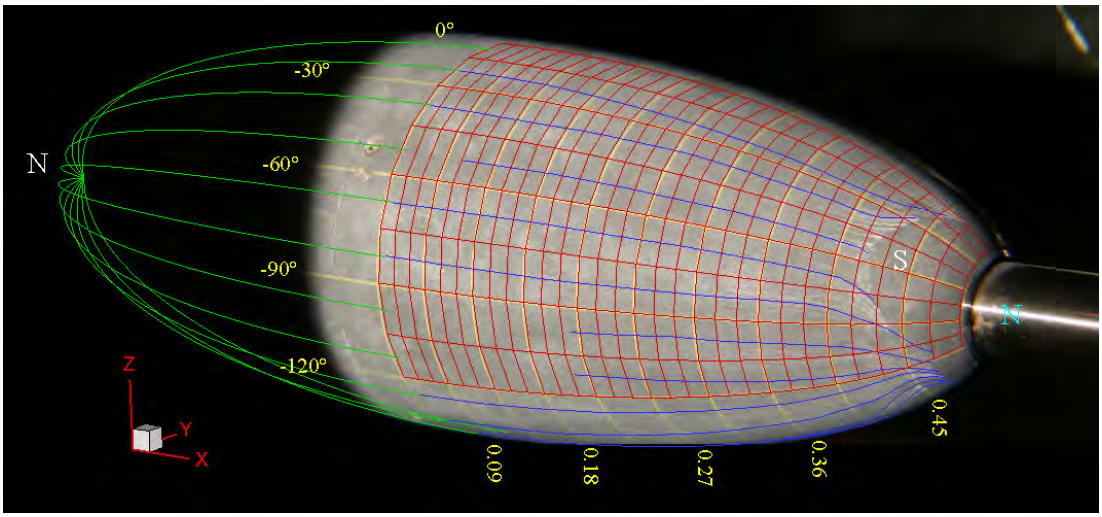

(a) Upper View

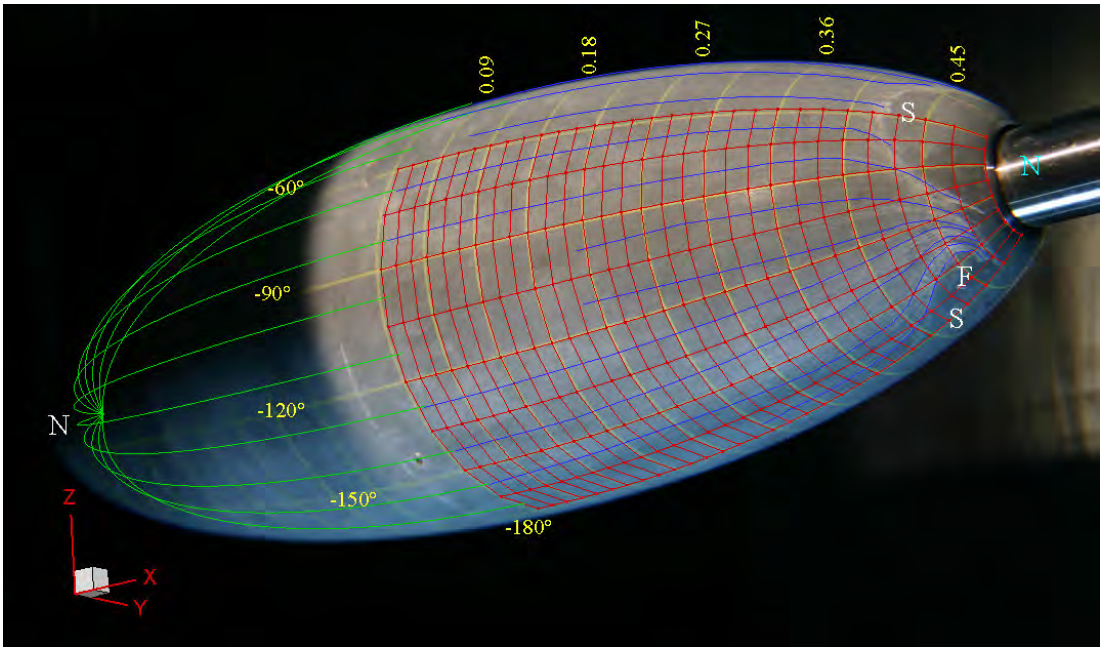

(b) Lower View

Figure 7.15: Surface flow visualisation on spheroid, $\alpha = -0.2°$, $Re_l = 4.0 \times 10^6$. The departure from axisymmetric flow seen over the last 10% of the spheroid is attributed to the lack of strong azimuthal gradients allowing usually minor influences such as surface roughness and/or the initial distribution of the oil mixture to effect the surface streamlines. (Axes aligned with body coordinates, streamwise grids marked with x_{bc}/l values, green surface streamlines calculated from classical potential theory, blue surface streamlines drawn from underlying photo.)

$Re_l = 4.0 \times 10^6$

The nature of some of the singularities has been marked on Fig. 7.15. The overall topology of the singularities can not be checked against the criteria that the number of nodes exceeds the number of saddles by two, as there no longer exists one plane of symmetry and flow visualisation is only available from one side.

The flow at $Re_l = 4.0 \times 10^6$ exhibits similar characteristics as seen for this slight angle of incidence at $Re_l = 2.0 \times 10^6$, notably that the surface streamlines are aligned with the grid until the last 10% of the model length, where the flow becomes non-axisymmetric. An earlier separation occurs centred at $\varphi = -50°$ which is downstream of one of the screws, but not at $\varphi = -140°$ downstream of another screw. It is also worth recalling that in the pressure measurements at this incidence at $Re_l = 3.5 \times 10^6$ the separation point was seen to move upstream towards $x_{bc}/l \approx 0.41$. It is possible that the earlier separation at higher Reynolds numbers is due to the disturbance caused by the pressure tappings (but not the screw heads as they are not in line with the pressure tappings). The earlier separation noted at $\varphi = -50°$ may result from a thicker boundary layer due to earlier laminar to turbulent transition of the boundary layer produced by the surface roughness. For tests with the ellipsoid the sockets in the screw heads were filled with setting silicone and the model with the pressure tappings was only used for the pressure measurements.

7.3 4.2–2–1 Ellipsoid Flow Visualisation

The same surface visualisation techniques applied to the spheroid were applied to these tests, but in general a slightly thinner coating of the oil mixture was applied. This tends to produce less visible surface streamlines on the body but better definition of the separation lines. Also, as previously noted, the screw sockets are filled to minimise disturbance to the flow. (For the model used with the boundary layer survey, snake-eye screws replaced the socket head screws as their two smaller holes are easier to fill.)

7.3.1 Ellipsoid at $\alpha = -10.2°$, Boundary Layer Tripped at 20% of Total Length

At $\alpha = -0.2°$ the potential streamlines show the node of attachment for the spheroid is almost isotropic, with all potential streamlines leaving at a different angle (Fig. 7.15). The corresponding node of attachment of the ellipsoid shows the potential streamlines leaving along a common tangent. (The only surface streamlines that leave at a different angle are those on the symmetry plane; these are not drawn.) Fig. 7.16 shows streamlines from the upstream node of attachment converging to a single line from both pressure and suction sides creating an open type separation. This open separation starts at $x_{bc}/l \approx 0.2$, $\varphi_e \approx -105°$ and continues along the flank of the model until it forms the pressure side of a closed separation at $x_{bc}/l \approx 0.31$, $\varphi_e \approx -90°$. This closed separation extends to the end of the body between $\varphi_e \approx -70°$ and $-110°$. The combination of open and closed separation on the flank prevents the surface streamlines converging towards a separation line at $x_{bc}/l \approx 0.48$, $\varphi_e \approx -120°$ as suggested by the potential calculations (Fig. 7.17). The surface streamlines diverge from the suction side towards the region of separated flow. An additional saddle ($x_{bc}/l \approx 0.44$, $\varphi_e \approx -110°$) and node ($x_{bc}/l \approx 0.47$, $\varphi_e \approx -115°$) occur when these surface streamlines from the suction side meet the region of separated flow. The surface topology has an additional saddle and node on each flank when compared to the corresponding case with the spheroid. This topological description of the surface still meets the requirement that the number of nodes exceeds the number of saddles by two. The flow visualisation on the suction side provides an excellent example of the open and closed separation on the flank of the model.

The separation line at $x_{bc}/l \approx 0.45$ between $\varphi_e = 0°$ and $\varphi_e \approx -60°$ appears two-dimensional, with no obvious deviation in the surface streamlines approaching it. On the suction side the separation is centred on the symmetry plane at $x_{bc}/l \approx 0.43$ and the separator line of the saddle connects to the node at $x_{bc}/l \approx 0.47$, $\varphi_e \approx -115°$.

A discontinuity exists between the potential and surface streamlines where they meet be-

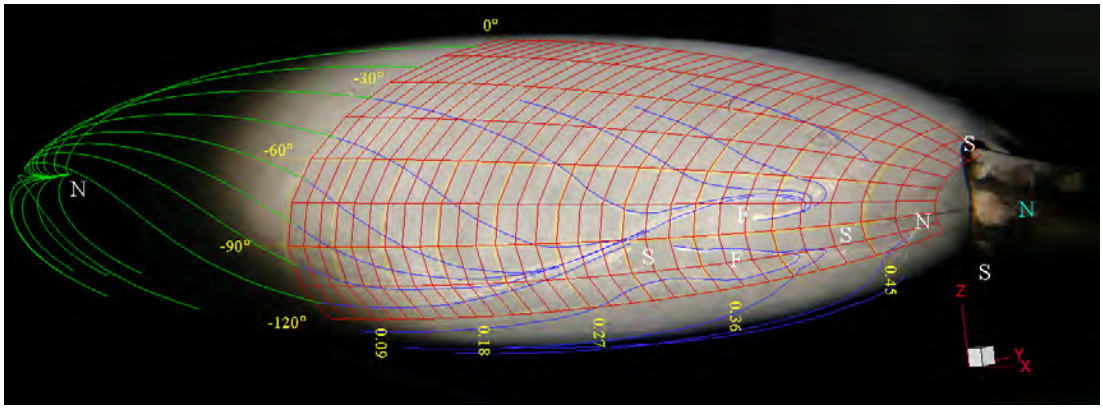

(a) Upper View

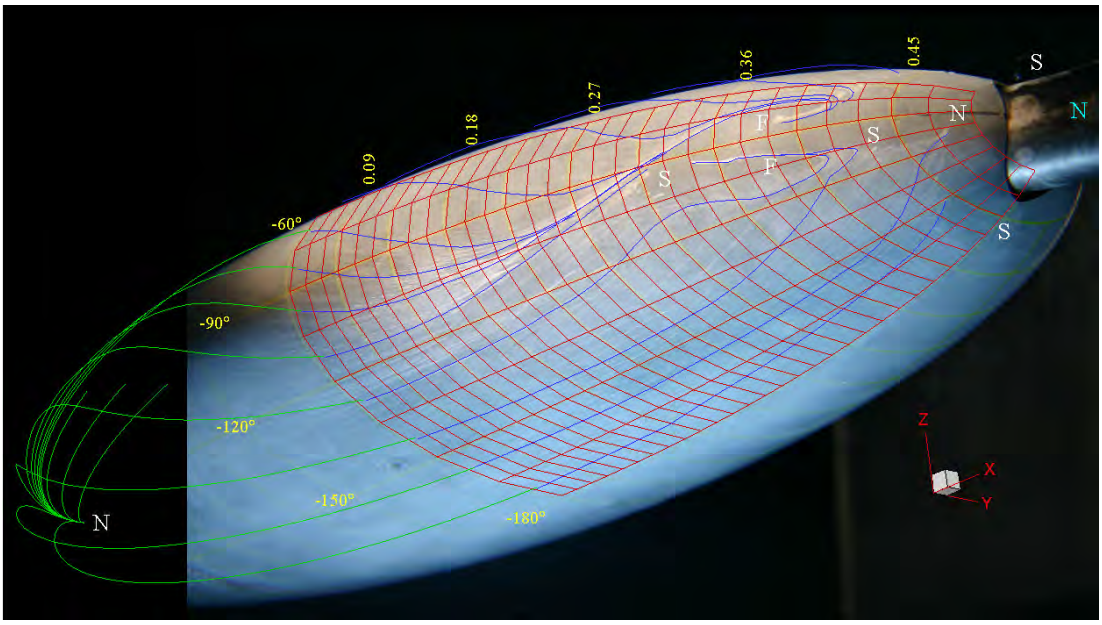

(b) Lower View

Figure 7.16: Surface flow visualisation on ellipsoid, $\alpha = -10.2°$, boundary layer tripped at $x_{bc}/l = -0.3$, $Re_l = 3.0 \times 10^6$. The convergence of surface streamlines starting at $x_{bc}/l \approx 0.2$, $\varphi_e \approx -105°$ indicates an open separation. (Azimuthal angles marked using φ_e, axes aligned with body coordinates, streamwise grids marked with x_{bc}/l values, green surface streamlines calculated from classical potential theory, blue surface streamlines drawn from underlying photo.)

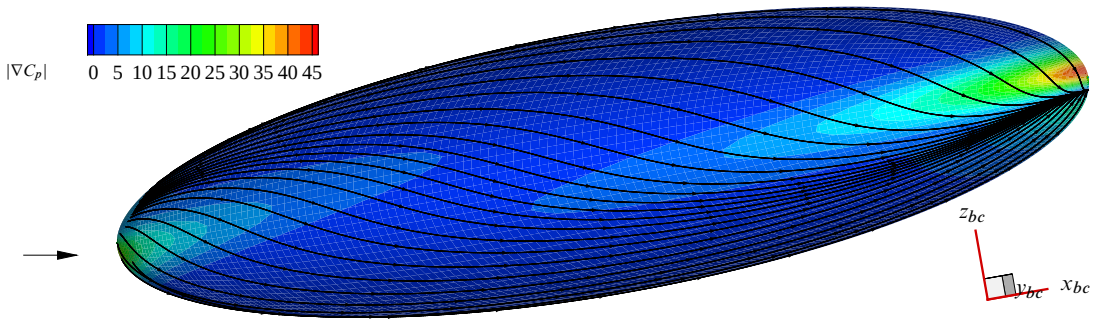

Figure 7.17: Potential streamlines and non-dimensionalisation by pressure gradient magnitude for ellipsoid at $\alpha = -10.2°$. (Non-dimensionalised on freestream dynamic pressure and model length)

tween $\varphi_e \approx -90°$ and $-135°$ where the surface streamlines are influenced by the azimuthal pressure gradient. Outside this region ($-60° > \varphi_e > -150°$) these potential and drawn surface streamlines are aligned.

7.3.2 Ellipsoid at $\alpha = -10.2°$

$Re_l = 2.0 \times 10^6$

The closed separation on the model's flank starts at $x_{bc}/l \approx 0.14$, $\varphi_e \approx -100°$ (Fig. 7.18). Upstream of this separation there is a convergence of surface streamlines from the suction side towards $x_{bc}/l \approx -0.04$, $\varphi_e \approx -110°$; a similar convergence at this location is seen in flow visualisation performed at $Re_l = 1.0 \times 10^6$. Photos taken in the sequence leading up to Fig. 7.18 show the separation on the flank of the body extending forward to this region of convergence, so the extent of this separation is sensitive to the observation time. The surface topology at this location is therefore not definitive.

A significant difference in the surface topology exists between this case and the one in Subsection 7.3.1 where the trip strip was employed. In this case the boundary layer stays attached until the end of the body on the pressure side. Fig. 7.18(a) shows a short laminar separation bubble near $x_{bc}/l = 0.41$ to 0.44 for φ_e between 0° and −45°. Flow visualisation using a more viscous mixture shows attached flow until the end of the body for φ_e between 0° and −30°.

When the entire model-sting interface is in a region of separated flow, the upstream flow along the surface of the sting is treated as a node of attachment for the model. In this case the topology at the model-sting interface is more complex. The flow leaving the end of the model on the pressure side appears to recirculate onto the model further towards the suction side.

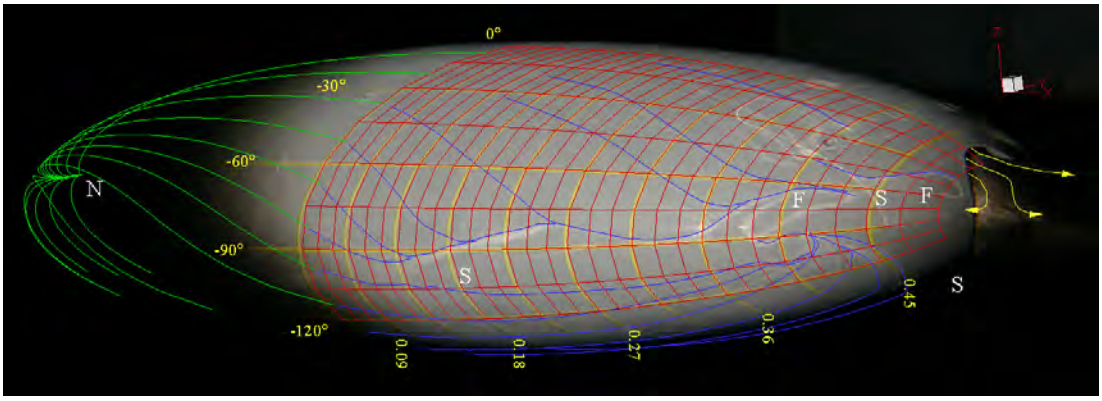

(a) Upper View, On the pressure side near the symmetry plane the boundary layer has stayed attached until the end of the ellipsoid.

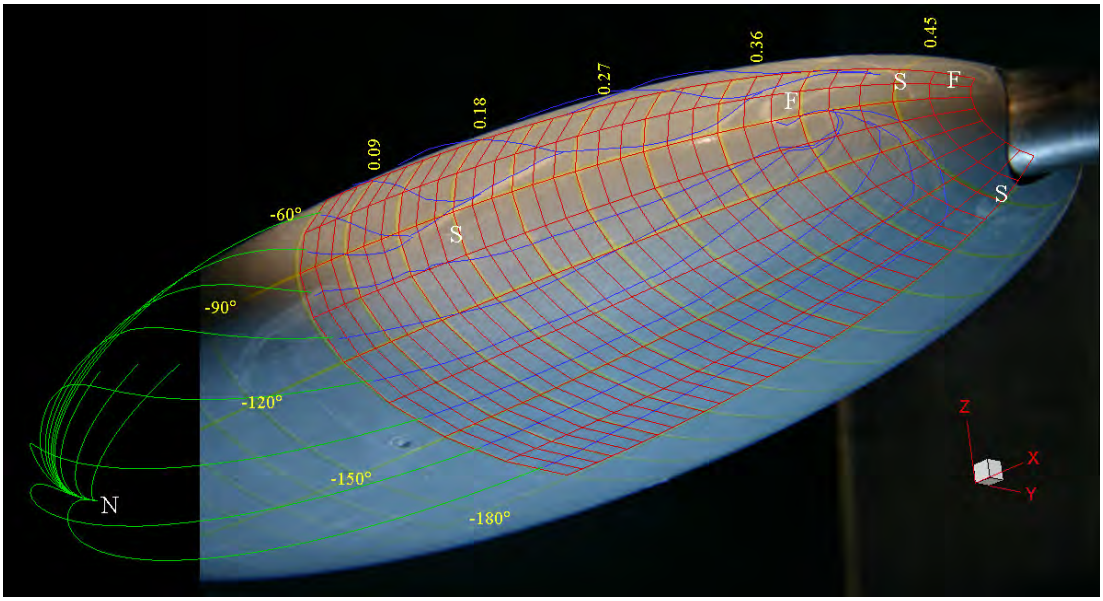

(b) Lower View, the extent of the open separation on the flank initially extended to $x_{bc}/l \approx -0.04$ but later shifted downstream to $x_{bc}/l \approx 0.14$

Figure 7.18: Surface flow visualisation on the ellipsoid, $\alpha = -10.2°$, $Re_l = 2.0 \times 10^6$. A single focus dominates the separation on the flank at $x_{bc}/l \approx 0.40$. (Yellow arrows indicating expected flow direction from end of model, azimuthal angles marked using φ_e, axes aligned with body coordinates, streamwise grids marked with x_{bc}/l values, green surface streamlines calculated from classical potential theory, blue surface streamlines drawn from underlying photo.)

The yellow arrows in Fig. 7.18(a) indicate the expected path of the flow leaving the end of the model near the pressure side of the symmetry plane.

The separation on the flank of the model is dominated by a single focus rather than a pair of counter rotating foci on either side of the separated region. Also in comparison to the case when the boundary layer was tripped:

- a saddle and focus are visible on the pressure side of this separation rearward of the main foci ($\varphi_e = -90°$, $x_{bc}/l = 0.4$) instead of a saddle and node on the suction side. It is possible that a saddle and node/foci exist on the suction side but have not been detected due to a lack of oil mixture in this region. (A saddle and node is apparent in some of the photos on the suction side rearward of the main foci for $\alpha = -10.2°$, $Re_l = 2.5 \times 10^6$).
- the separation on the suction side occurs further downstream at $x_{bc}/l \approx -0.45$. The angle between the separator line from the saddle on the symmetry plane and the model's azimuthal grid lines for φ between $-120°$ and $-150°$ is smaller. The later separation may be explained by a thinner boundary layer on the suction side, as the laminar to turbulent transition is occurring further downstream.

An incomplete topology for the singularities is evident in Fig. 7.18, as the number of nodes does not exceed the number of saddles by two.

$Re_l = 2.5 \times 10^6$

The flow around the front of this model is observed at $Re_l = 2.5 \times 10^6$ in Fig. 7.19(a). The influence of the pressure gradient on the low inertia fluid near the surface is apparent for φ_e between $-30°$ and $-120°$ near the front of the model. The surface streamlines show the azimuthal pressure gradients' greater influence on the direction of low inertia flow near the surface to that of the bulk flow as indicated by the potential streamlines. A significant change in flow direction occurs across the height of the boundary layer. Numerical solutions, both laminar and turbulent, show the position of the forward node of attachment is only fractionally shifted from the position calculated by the potential solution. The tangent line emanating from this node is close to identical for the potential, laminar and turbulent solutions.

The lower view (Fig. 7.19(c)) for this case shows a significant kink in the flow near $x_{bc}/l \approx 0$ for $\varphi_e \approx -105°$. This is in the same region where the convergence of surface streamlines was observed for this incidence at $Re_l = 2.0 \times 10^6$. Fig. 7.20 shows the streamlines overlaid on a three-dimensional contour plot of the surface C_p along with a curve showing the location of transition as determined from the boundary layer survey ($\bar{\gamma}_{0.25}$ - see Chapter 8 for details). The contour plot is constructed from data points at the intersections of the grid lines; the range is restricted to provide greater resolution in the low pressure area of interest.

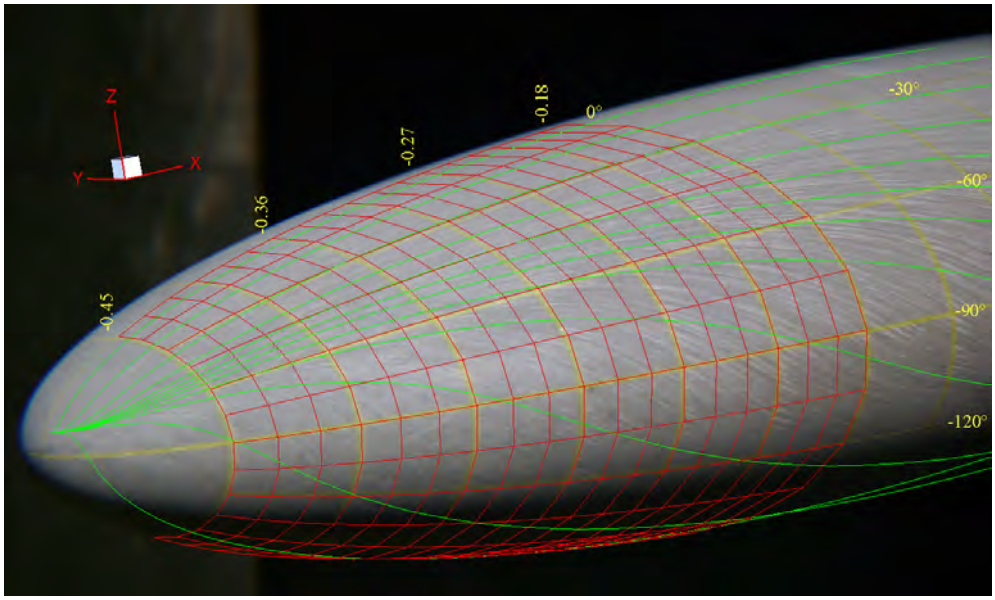

(a) Front View

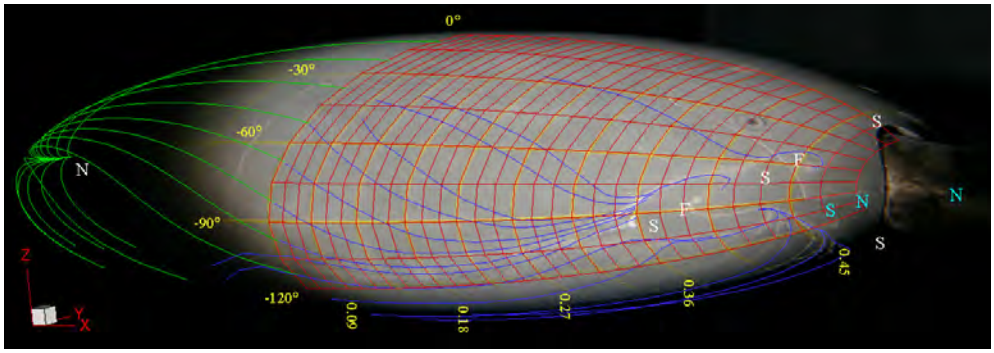

(b) Upper View

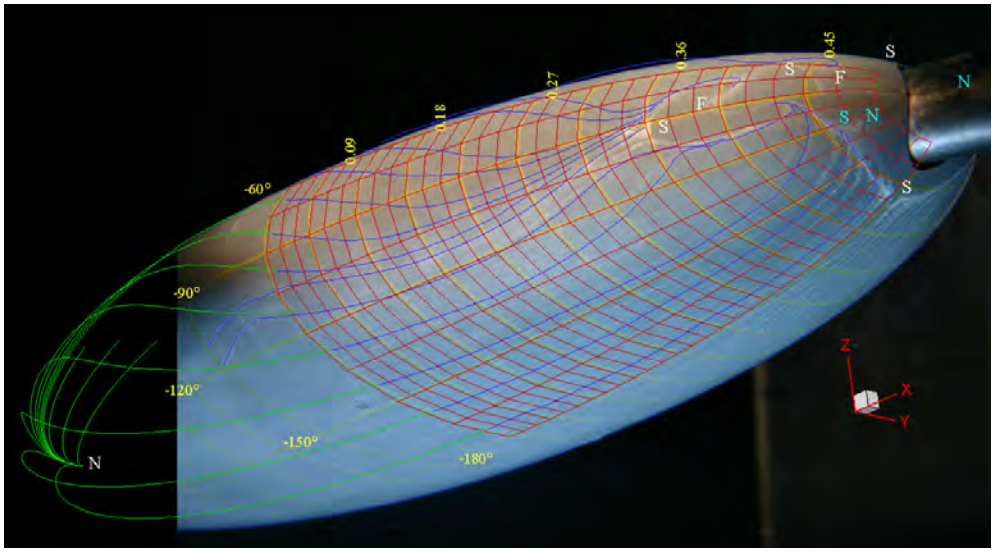

(c) Lower View

Figure 7.19: Surface flow visualisation on ellipsoid, $\alpha = -10.2°$, $Re_l = 2.5 \times 10^6$. (See caption of Fig. 7.18)

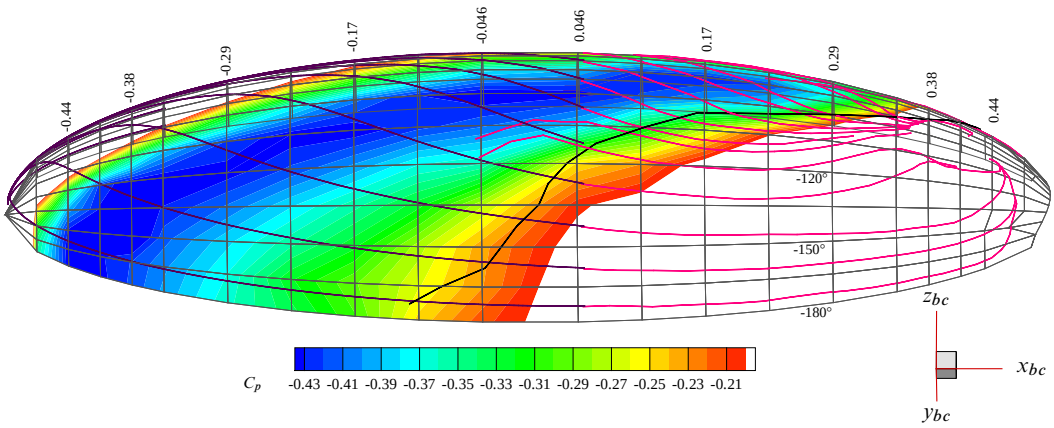

Figure 7.20: Plot of measured C_p for ellipsoid at $\alpha = -10.2°$. The perturbations in the surface streamlines near $x_{bc}/l \approx 0$, $\varphi_e \approx -105°$ traced from the flow visualisation are situated close to where boundary layer transition was measured. Potential streamlines (purple), surface streamlines (pink), and boundary layer transition line (dark grey).

The low pressure region near $x_{bc}/l \approx 0$, $\varphi_e \approx -90°$ may be responsible for the kink, but this explanation is considered less likely as a band of low pressure of similar magnitude exists from $x_{bc}/l \approx -0.44$ to -0.30 without similar influences on the surface streamlines being observed. Boundary layer transition may be responsible for this kink. Similar deviations in the surface streamlines are seen in the flow visualisation performed on the spheroid at $\alpha = -6.2°$ and $-10.2°$ at this Reynolds number. This kink is localised, as a short distance away the potential and surface streamlines have a similar direction.

The overall topology is similar to that seen at $Re_l = 2.0 \times 10^6$ except that:

- the boundary layer on the pressure side of the symmetry plane separates a short distance before the end of the model, at $x_{bc}/l \approx 0.46$, so a saddle occurs at this location.
- associated with this earlier separation, the saddle and foci on the pressure side of the model have moved upstream so the foci is no longer positioned at base of the model.
- an additional saddle and node were seen in the initial photos in this sequence on the suction side of the separation near the sting. The remains of this saddle and node are visible in the photo, and the associated node and saddle are indicated in cyan letters.

If the oil-flow visualisation provides a premature estimate of separation, as suggested by Squire [68], the flow on the pressure side may stay attached until the end of the model. The topology of the singularities shown in Fig. 7.19 does not meet the requirements that the number of nodes exceed the number of saddles by two. Additional singularities may exist in the separated region and not be detected due to a lack of oil and/or their small size.

Near the hatch ($x_{bc}/l \approx 0.31$, $\varphi_e \approx -30°$) in Fig. 7.19(b) some arcs are visible in the oil mixture, approximately perpendicular to the flow direction . These arcs are a remnant from the direction the cutter was heading during manufacturing. No discontinuity in the surface can be felt by finger tips over this region.

$Re_l = 3.0 \times 10^6$

At $Re_l = 3.0 \times 10^6$ the flow on the pressure side stays attached until the end of the model over a similar azimuthal extent as seen at 2.0×10^6. Except for the lack of the open separation the flow topology is very similar to that seen at 2.0×10^6. Fig. 7.21 shows the visualisation performed with different viscosities and quantities of oil mixture.

$Re_l = 4.0 \times 10^6$

A comparison between this case and when the trip strip was employed at this incidence (Fig. 7.16) shows:

- the topology of the identified singularities is the same;
- the location of the separation on the suction and pressure side of the model is almost identical;
- convergence of the surface streamlines for φ_e between $-60°$ and $-120°$ is less and no open separation occurs in this region;
- separation on the flank of the model occurs at a similar azimuth ($\varphi_e \approx -100°$) though further downstream, starting at $x_{bc}/l \approx 0.34$ instead of 0.31.

7.3.3 Ellipsoid at $\alpha = -6.2°$

$Re_l = 2.0 \times 10^6$

An open separation line leads to a closed separation starting at $x_{bc}/l \approx 0.42$, $\varphi_e \approx -80°$ (Fig. 7.23). Care needs to be exercised when examining this photo as there is a concentration of oil mixture near $x_{bc}/l \approx 0.04$, $\varphi_e \approx -110°$ that is moving downstream. A surface streamline has been drawn through this region to indicate the skin friction direction (Fig. 7.23(b)). The surface streamline of the open separation joins the separator line from the saddle on the pressure side. This closed separation starts downstream ($x_{bc}/l \approx 0.14$) of the corresponding flank separation at $\alpha = -10.2°$ for the same Reynolds number.

The flow stays attached on the pressure side near the symmetry plane until the end of the body for φ_e between $0°$ and approximately $-10°$. The topology of the identified singularities

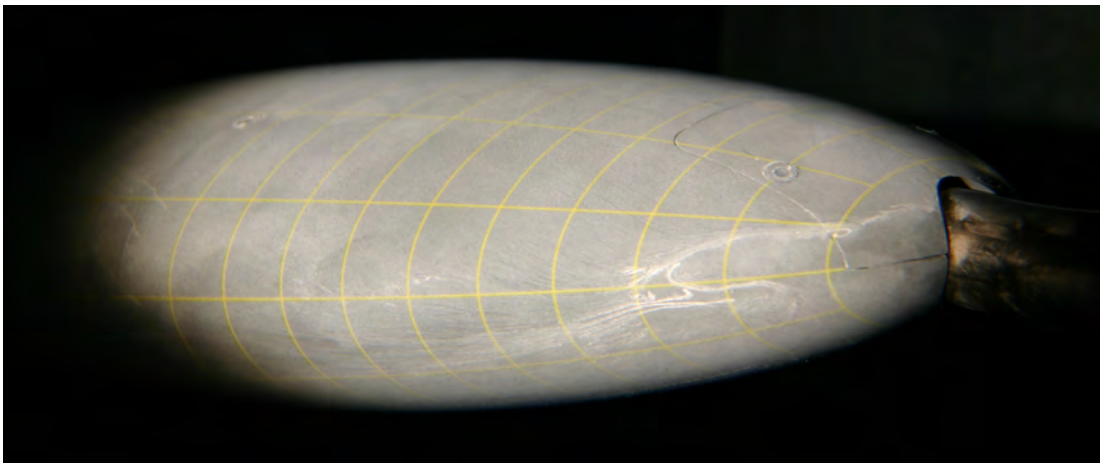

(a) Dow Corning® 200 fluid **5000** cSt, thin layer

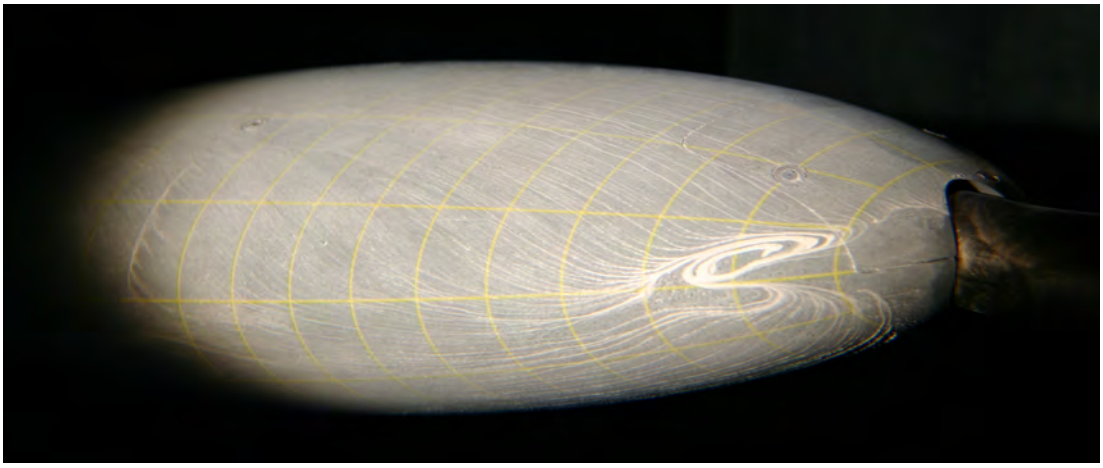

(b) Dow Corning® 200 fluid **1000** cSt, thick layer

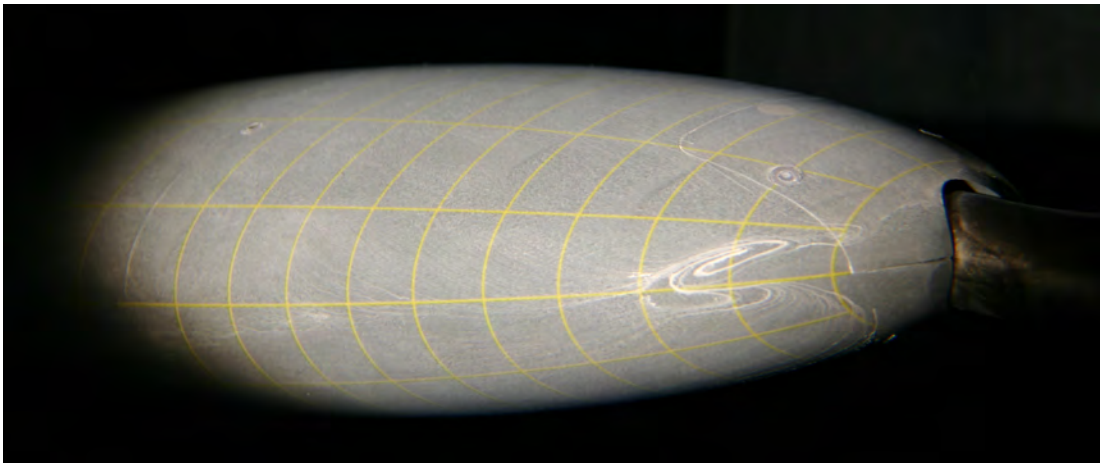

(c) Dow Corning® 200 fluid **1000** cSt, thin layer

Figure 7.21: Different viscosity oil mixtures along with the thickness of application influence the visibility of the surface features. Upper View, $\alpha = -10.2°$, $Re_l = 3.0 \times 10^6$, $22.3°C$

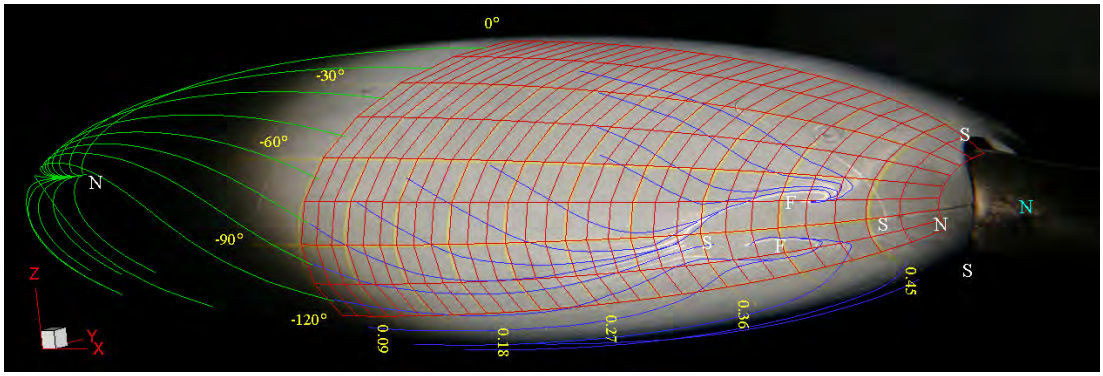

(a) Upper View

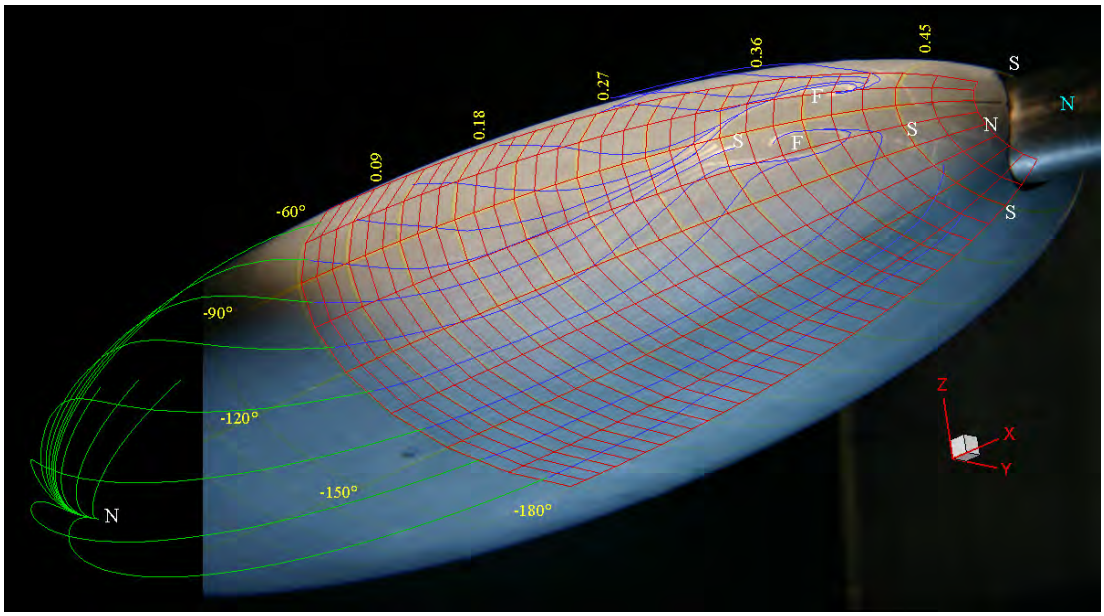

(b) Lower View

Figure 7.22: Surface flow visualisation on ellipsoid, $\alpha = -10.2°$, $Re_l = 4.0 \times 10^6$. Flow separation occurs prior to the end of the model on the pressure side. No open separation is apparent. When the trip strip was used at this incidence for $Re_l = 3.0 \times 10^6$ the limiting surface streamline of the open separation was visible. (Azimuthal angles marked using φ_e, axes aligned with body coordinates, streamwise grids marked with x_{bc}/l values, green surface streamlines calculated from classical potential theory, blue surface streamlines drawn from underlying photo.)

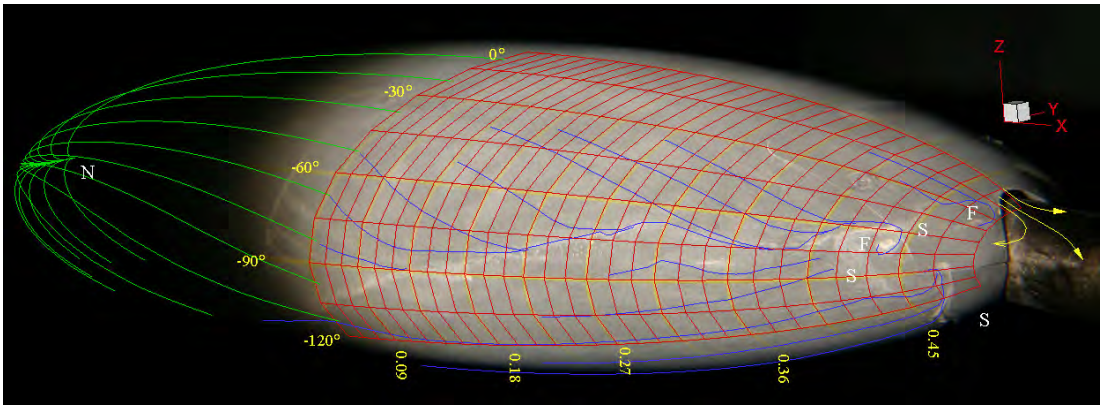

(a) Upper View

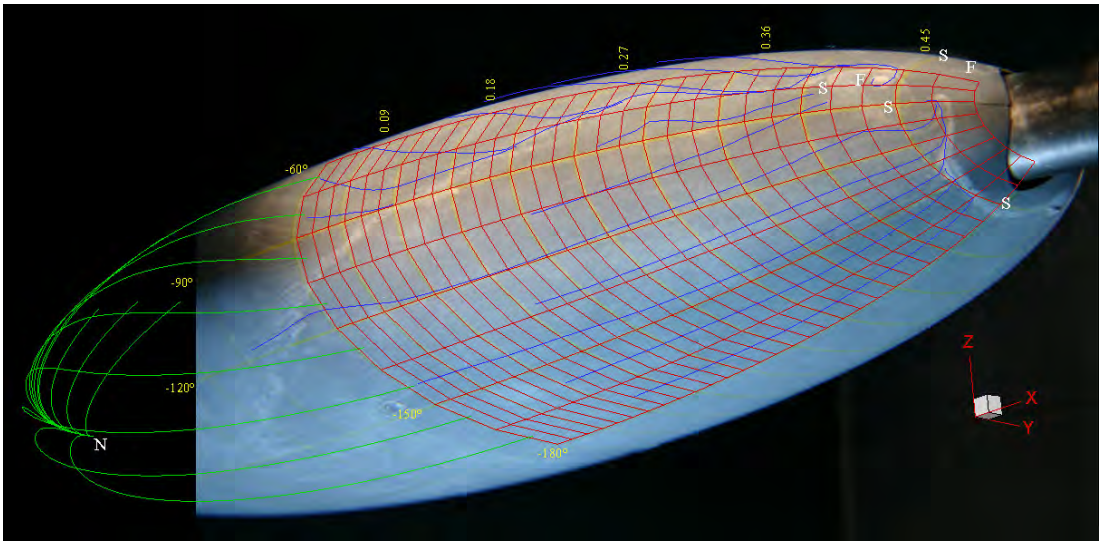

(b) Lower View

Figure 7.23: Surface flow visualisation on ellipsoid, $\alpha = -6.2°$, $Re_l = 2.0 \times 10^6$. The separation on the flank is smaller than for the corresponding Reynolds number when $\alpha = -10.2°$. There is a concentration of oil mixture near $x_{bc}/l \approx 0.04$, $\varphi_e \approx -110°$ that is moving downstream. (Yellow arrows indicating expected flow direction from end of model, azimuthal angles marked using φ_e, axes aligned with body coordinates, streamwise grids marked with x_{bc}/l values, green surface streamlines calculated from classical potential theory, blue surface streamlines drawn from underlying photo.)

is the same as for this Reynolds number at $\alpha = -10.2°$. There appears to be an end of the separator line from the saddle on the suction side of the symmetry plane at $x_{bc}/l \approx 0.47$, $\varphi_e \approx -90°$ that is not marked as a node. The flow is believed not to leave the surface at this location, but to move upstream in the separated region towards the main focus on the flank of the body. This description is consistent with the surface streamline patterns observed in this region for this incidence at $Re_l = 2.5 \times 10^6$. The boundary layer separation near the symmetry plane on the suction side occurs near $x_{bc}/l \approx 0.45$ for $Re_l = 2.0 \times 10^6$, 2.5×10^6 and 3.0×10^6 at this incidence.

$Re_l = 2.5 \times 10^6$

The visualisation shows the azimuthal pressure gradients' influence on the low inertia flow around the nose. The flow visualisation at the rear of the model is very similar to that at $Re_l = 2.0 \times 10^6$. The most notable difference is that the open separation starts further downstream ($x_{bc}/l \approx 0.16$, $\varphi_e \approx -90°$) and the surface streamlines approaching this separation line do so at a smaller angle. The separator line from the saddle on the suction side is seen to terminate at the focus on the flank of the model. An incomplete topology of singularities is evident. The results at $Re_l = 3.0 \times 10^6$ appear similar to those seen here, but with no open separation on the flank.

The cyan line on Fig. 7.24(b) shows a kinked surface streamline ($x_{bc}/l \approx 0.31$, $\varphi_e \approx -20°$), that is a result of a small leak at the hatch. The leak was first noticed[1] while processing the data for $Re_l = 4.0 \times 10^6$. The leak will result in a flow from the interior to the exterior at the most upstream section of the hatch (best seen in Fig. 7.28 where air can be seen leaking from two small sections). If the flow is laminar the leak may destabilise the boundary layer, thus leading to premature transition. It is not expected to have a noticeable influence on the separations on the flank of the model.

Another test at this incidence and Reynolds number is marred by a small piece of debris caught at the junction between front and rear shells. The height of this piece is unknown but appears small. The mixing it causes and the resulting scour (Fig. 7.25) demonstrate the existence of a significant change in flow angle over the height of the debris.

$Re_l = 4.0 \times 10^6$

The boundary layer on the pressure side at $Re_l = 4.0 \times 10^6$ separates at $x_{bc}/l \approx 0.45$ for $0° \geqslant \varphi_e \gtrapprox -60°$. The boundary layer separation on the suction side extends from $\varphi_e = -180°$ to near $-120°$ and occurs near $x_{bc}/l \approx 0.45$. These separations appear two-dimensional for the

[1]This was after the cavitation tunnel had been decommissioned for an upgrade. This leak only influences the results at this incidence as the model was dismantled to change incidence and then resealed.

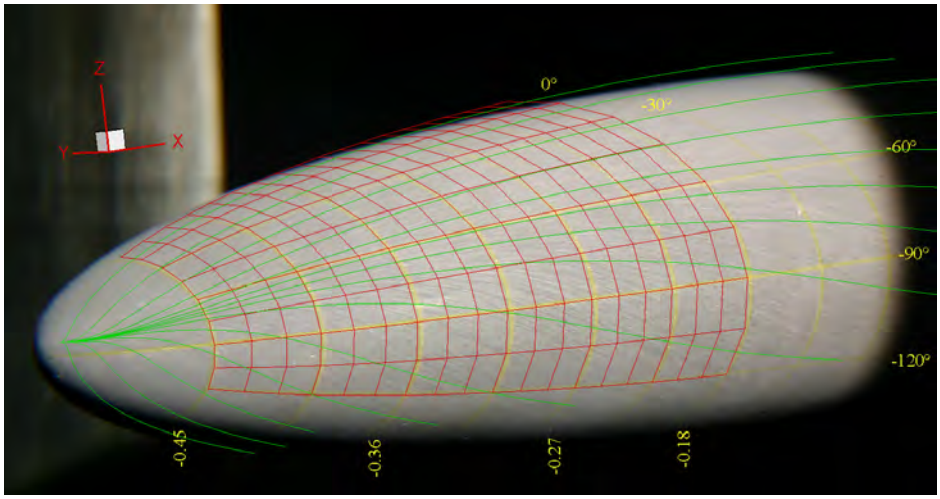

(a) Front View, the different direction between the potential streamlines (green) and the lines in the oil mixture show the azimuthal pressure gradients' influence on the low inertia flow around the nose.

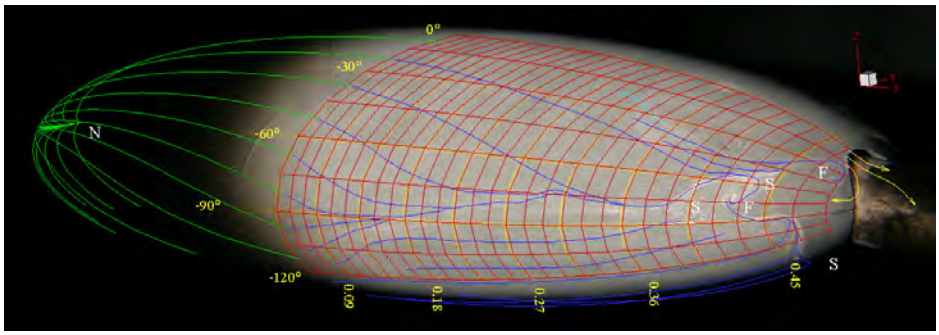

(b) Upper View, a small leak near the hatch occurs near $x_{bc}/l \approx 0.31$, $\varphi_e \approx -20°$) is indicated by the cyan line.

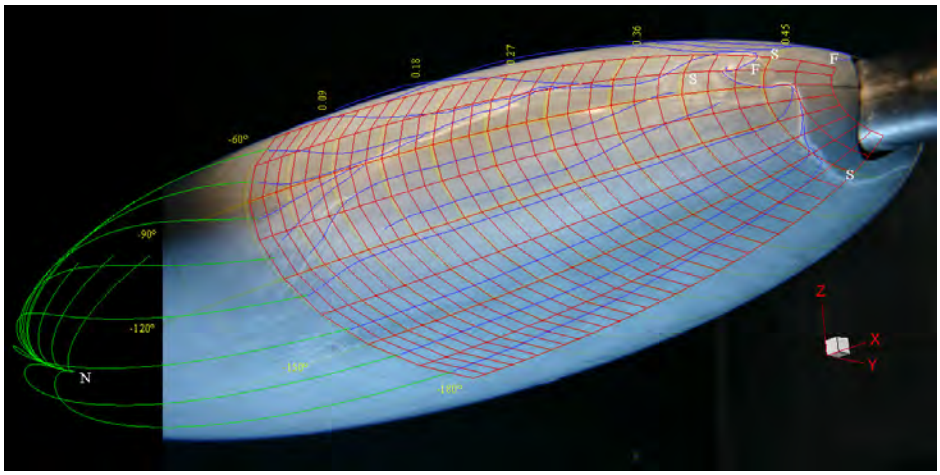

(c) Lower View

Figure 7.24: Surface flow visualisation on ellipsoid, $\alpha = -6.2°$, $Re_l = 2.5 \times 10^6$. (Yellow arrows indicating expected flow direction from end of model, azimuthal angles marked using φ_e, axes aligned with body coordinates, streamwise grids marked with x_{bc}/l values, green surface streamlines calculated from classical potential theory, blue surface streamlines drawn from underlying photo.)

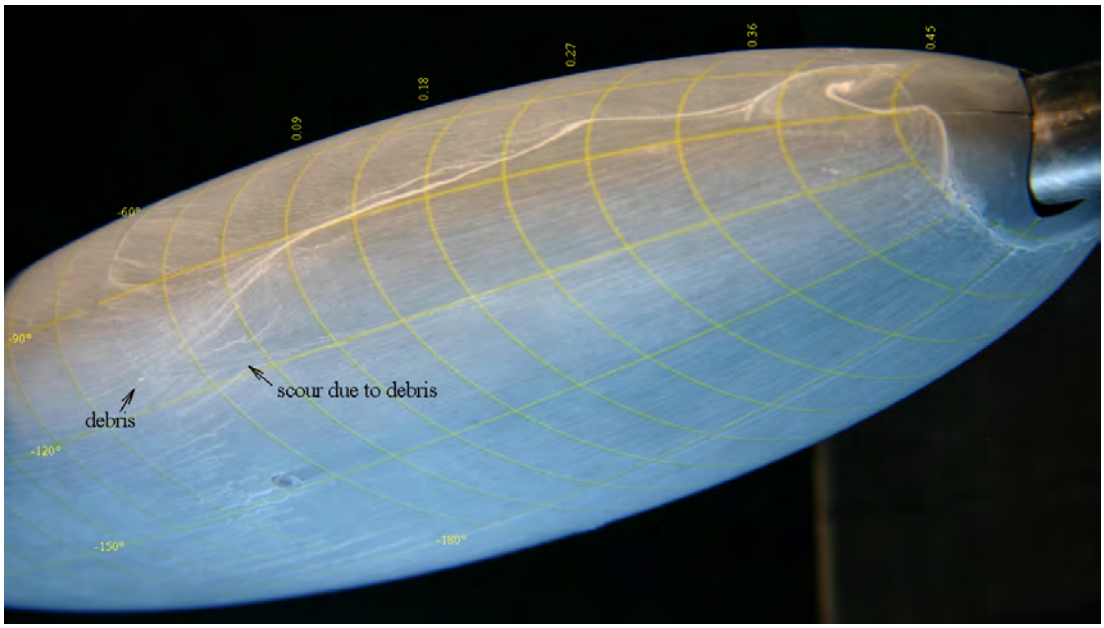

Figure 7.25: Scour mark on suction side of ellipsoid caused by a piece of debris, most likely a small flake of silicone sealant not cleaned off after the previous sealing, $\alpha = -6.2°$, $Re_l = 2.5 \times 10^6$.

region $0° \geqslant \varphi_e \gtrapprox -45°$ and $-135° \gtrapprox \varphi_e \geqslant -180°$. No open separation precedes the separation on the flank; this has a saddle near $x_{bc}/l \approx 0.39$, $\varphi_e \approx -80°$ and is dominated by a focus at $x_{bc}/l \approx 0.42$, $\varphi_e = -68°$.

The topology shown in Fig. 7.26 is incomplete, with the same number of nodes and saddles evident. The separation on the flank is dominated by the focus.

7.3.4 Ellipsoid at $\alpha = -0.2°$

$Re_l = 2.5 \times 10^6$

At $\alpha = -0.2°$ the plane $z_{bc} = 0$ should approach a plane of symmetry for the flow. The flow visualisation on the front of the model is not as clear as for other incidences at the front, so surface streamlines have been marked on the surface in blue as determined from the photo. This visualisation shows the low inertia fluid close to the surface is again influenced by the azimuthal pressure gradient (Fig. 7.27(a)). In this case, with minimal incidence, the azimuthal pressure gradients are less and the differences between the flow directions seen from the oil mixture and the potential streamlines are smaller.

The potential and drawn surface streamlines are parallel at the centre of the body. This is consistent with the zero azimuthal pressure gradient calculated from potential theory at

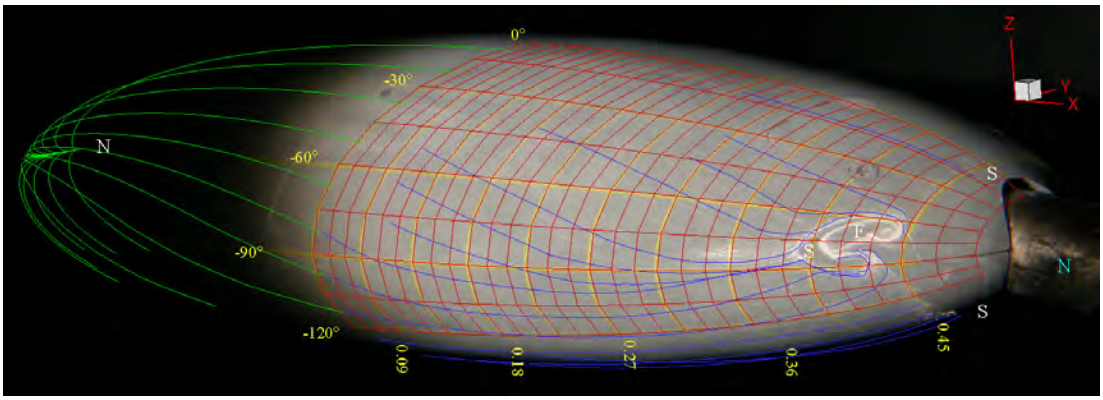

(a) Upper View

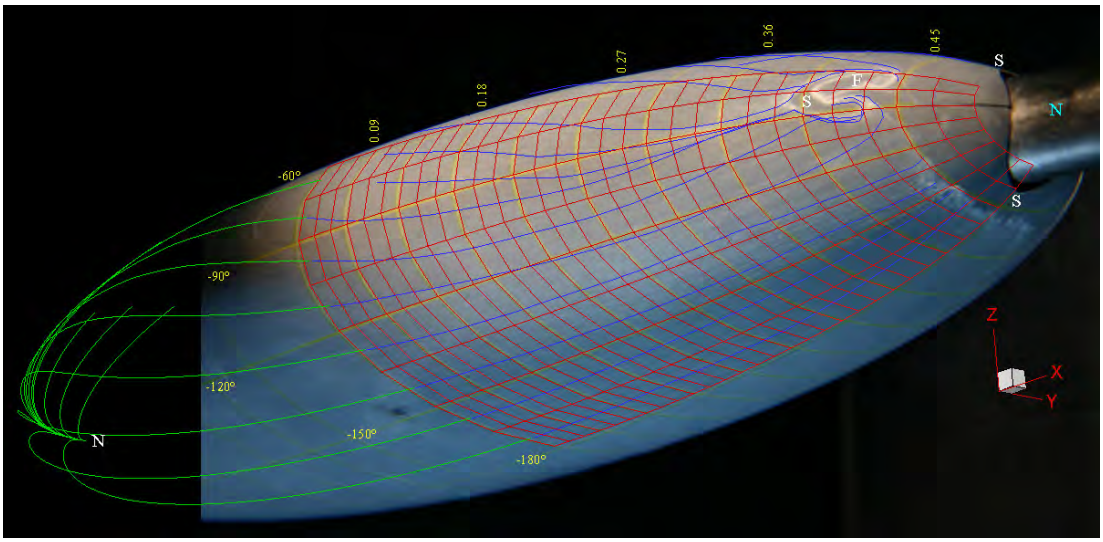

(b) Lower View

Figure 7.26: Surface flow visualisation on ellipsoid, $\alpha = -6.2°$, $Re_l = 4.0 \times 10^6$. The open separation that was visible at $Re_l = 2.0 \times 10^6$ and 2.5×10^6 is no longer present. (Azimuthal angles marked using φ_e, axes aligned with body coordinates, streamwise grids marked with x_{bc}/l values, green surface streamlines calculated from classical potential theory, blue surface streamlines drawn from underlying photo.)

$x_{bc}/l = 0$ for all φ_e at $\alpha = 0°$. The flow stays attached until the end of the body for φ_e between $0°$ to $-20°$ and $-160°$ to $-180°$. The remaining section experiences significantly varying extents of separation. The separation reaches its most upstream point near $x_{bc}/l = 0.4$ at $\varphi_e = -45°$ and $-135°$. The flow between $\varphi_e = -60°$ and $-120°$, where it is subject to the significant length of adverse pressure gradient (Fig. 7.29), stays attached until $x_{bc}/l \approx 0.48$. Earlier separation of the flow near $\varphi_e = -45°$ and $-135°$ prevents the surface streamlines from converging at $\varphi_e = -90°$, as suggested by the potential solution, and allows the thinner boundary layer to stay attached for a greater distance.

The focus at the rear of the model seen from the upper view appears smaller, closer to

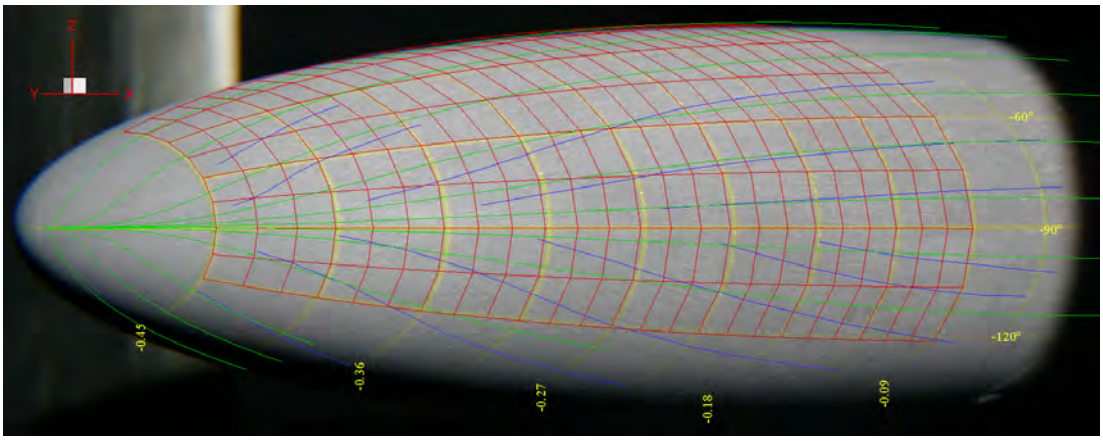

(a) Front View

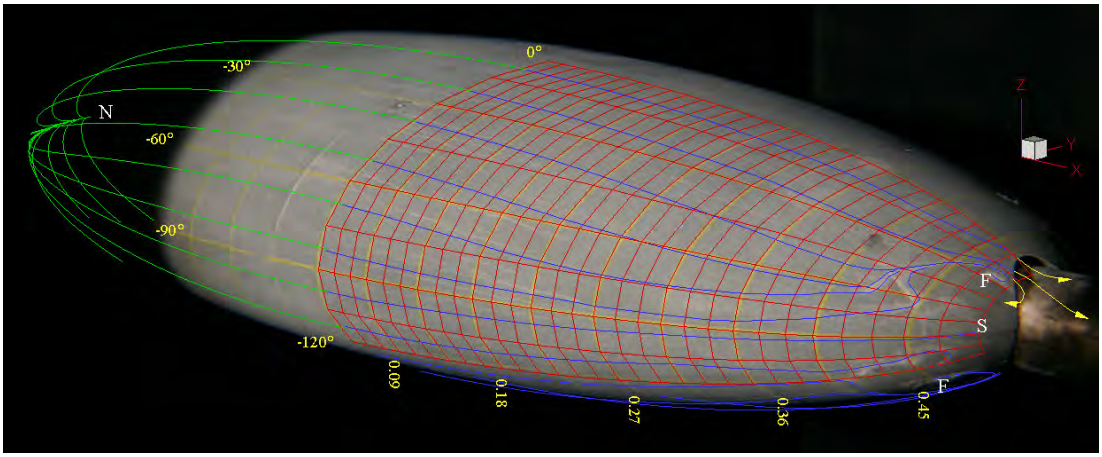

(b) Upper View

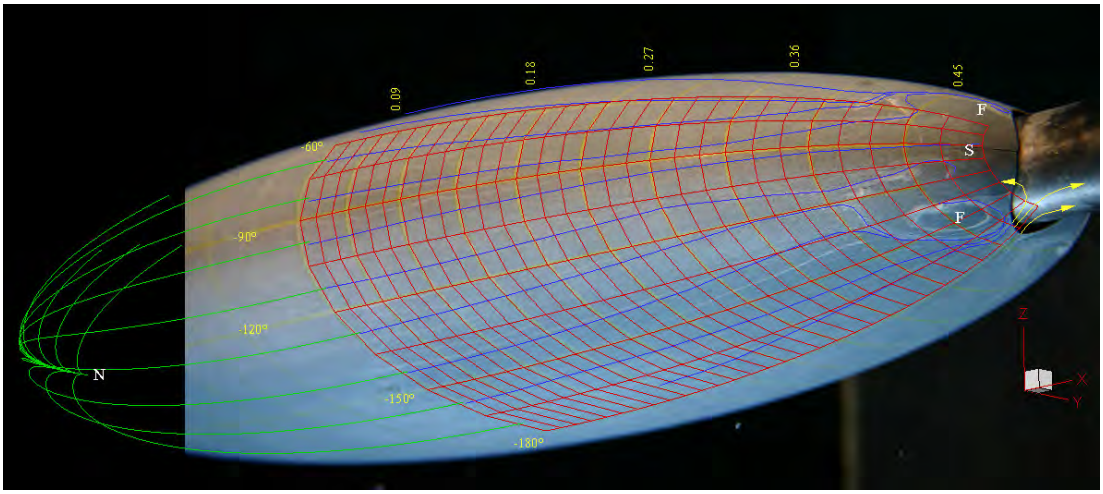

(c) Lower View

Figure 7.27: Surface flow visualisation on ellipsoid, $\alpha = -0.2°$, $Re_l = 2.5 \times 10^6$. The flow near $\varphi_e = -90°$ is attached until $x_{bc}/l = 0.47$ despite a significant length of adverse pressure gradient. (See caption of Fig. 7.24)

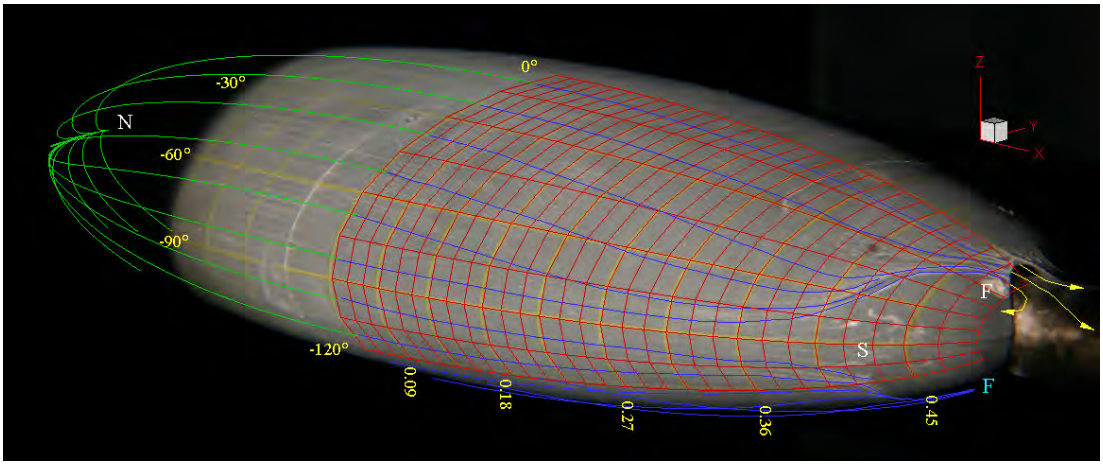

(a) Upper View

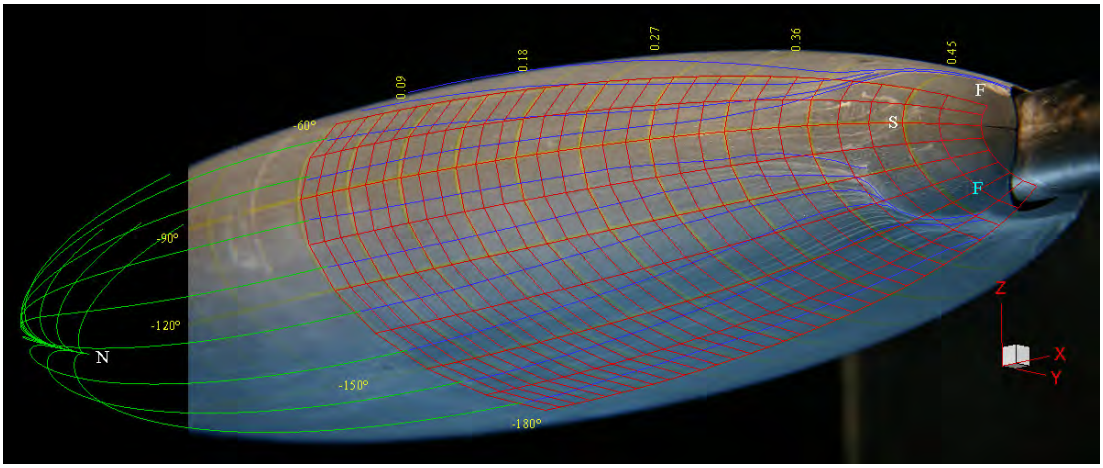

(b) Lower View, The lack of a foci near $x_{bc}/l \approx 0.48$, $\varphi_e = -150°$, is at odds with the visualisation on the other three quadrants.

Figure 7.28: Surface flow visualisation on ellipsoid, $\alpha = -0.2°$, $Re_l = 4.0 \times 10^6$. The flow near $\varphi_e = 0°$ is attached at the end of the model. At $\varphi_e = -180°$ the flow appears to separate marginally before the end of the model. (Yellow arrows indicating expected flow direction from end of model, azimuthal angles marked using φ_e, axes aligned with body coordinates, streamwise grids marked with x_{bc}/l values, green surface streamlines calculated from classical potential theory, blue surface streamlines drawn from underlying photo.)

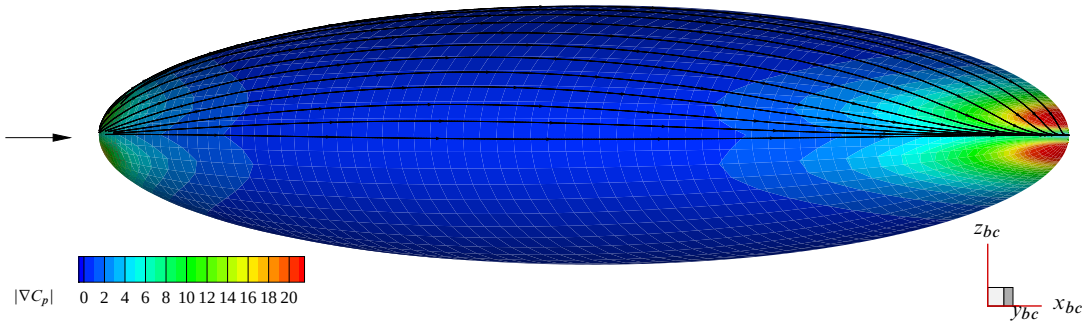

Figure 7.29: Potential streamlines and non-dimensionalised pressure gradient magnitude for ellipsoid at $\alpha = -0.2°$. (Model rotated 30° about z-axis, Non-dimensionalised on freestream dynamic pressure and model length)

the symmetry plane and further downstream than the one seen in the lower view (Fig. 7.27). The most significant difference between this flow topology and those seen previously is the attachment of the flow near both sides of the $y_{bc} = 0$ symmetry plane at the end of the model. The topology of the identified singularities is incomplete, in part due to the lack of visualisation on the sting.

$Re_l = 4.0 \times 10^6$

The visualisation performed at this incidence and Reynolds number was subject to occasional variability; demonstrating the sensitivity of the flow (or at least the flow visualisation) to minimal disturbances when significant azimuthal pressure gradients are not present. In the separated region the lower view shows a focus developed on the far side of the $y_{bc} = 0$ plane but not closest to the camera. The upper view shows the existence of a focus in the separated region at the base closest to the camera and enough of the far side to believe another one was present there. Given that there are two planes (approximately) of flow symmetry it is reasonable to expect four foci would ideally exist as seen at $Re_l = 2.5 \times 10^6$.

The most upstream location of the separation occurs at $x_{bc}/l \approx 0.42$, $\varphi_e = -75°$. The flow near $\varphi_e = -90°$ separates earlier than was the case for $Re_l = 2.5 \times 10^6$ at this incidence, $x_{bc}/l \approx 0.44$ instead of $x_{bc}/l \approx 0.48$. There is a significant adverse pressure gradient between these locations. The flow near $\varphi_e = 0°$ is attached at the end of the model. At $\varphi_e = -180°$ the flow appears to separate marginally before the end of the model, though given the unusual visualisation in this vicinity no conclusions are drawn from this observation. Given Squire's [68] studies the greater quantity of oil at this location may be influencing the observation.

The upper surface topology of singularities is similar to that seen at $Re_l = 2.5 \times 10^6$.

7.4 Summary

For both the spheroid and ellipsoid the largest regions of boundary layer separation were present when $\alpha = -10.2°$ and the Reynolds numbers were at the maximum ($\approx 4.0 \times 10^6$). Open separations of the flow were apparent at the lower Reynolds numbers tested ($Re_l = 2.0 \times 10^6$ and 2.5×10^6) for the ellipsoid at incidence ($\alpha = -6.2°$ and $-10.2°$). Open separations were not apparent on the spheroid at any incidence or Reynolds number tested.

The largest regions of separated flow occurring at the maximum Reynolds number on the spheroid are consistent with an earlier transition resulting in a thicker boundary layer. This thicker boundary layer is more likely to detach in regions of adverse pressure gradient. No visualisation was successful at $Re_l = 0.6 \times 10^6$ (and minimal success was achieved at 1.0×10^6) where large regions of laminar separation were apparent in the surface pressure measurements.

Flow visualisation on the spheroid shows a deviation in the surface streamlines near where transition is believed to occur in a number of cases. These perturbations are noticeable when minimal pressure gradients exist due to other influences, e.g. surface curvature or incidence. These perturbations may be confined close to the surface, and when thus confined provide an indicator of local conditions.

The flow visualisation on the ellipsoid at $\alpha = -10.2°$, $Re_l = 4.0 \times 10^6$ and with the boundary layer tripped (Fig. 7.5) provides an excellent example of the combination of open and closed separation on the flank of the model preventing the convergence of the surface streamlines on the suction side of the model near $\varphi_e = -120°$. This allows the surface streamlines between $\varphi_e = -120°$ and $\varphi_e = -180°$ to diverge as they approach the sting, thus allowing the flow on this side to stay attached until close to the sting. Similar extents of attached flow on the suction (and pressure) side are observed when no trip strip is used at this incidence, though the level of flow convergence on the flank of the model is less and no open separation is apparent.

At $\alpha = 10.2°$ the extent of attached flow on the pressure side near the symmetry plane was seen to extend:

- to the full length of the body at $Re_l = 2.0 \times 10^6$, with short laminar bubble present near $x_{bc}/l = 0.41$ to 0.44.
- to $x_{bc}/l \approx 0.46$ at $Re_l = 2.5 \times 10^6$.
- the full length of the body at $Re_l = 3.0 \times 10^6$.
- to $x_{bc}/l \approx 0.45$ at $Re_l = 4.0 \times 10^6$.

An explanation for these observations is obtained by considering the boundary layer state and its thickness. At $Re_l = 2.0 \times 10^6$ the recently reattached turbulent boundary layer should be

relatively thin and energetic and is thus able to remain attached. At 2.5×10^6 the thinner laminar boundary layer stays attached longer; when it separates the adverse pressure gradient due to the curvature is greater and the boundary layer is unable to reattach. At $Re_l = 3.0 \times 10^6$ the transition of the boundary layer near the rear of the body allows the more energetic boundary layer to stay attached. At $Re_l = 4.0 \times 10^6$ the transition of the boundary layer has shifted forward, leading to a longer section of turbulent flow; the resulting thicker boundary layer separates when subjected to the adverse pressure at the rear of the body.

For the ellipsoid at $\alpha = -6.2°$ and $-10.2°$:

- as the Reynolds number increases from 2.0×10^6 to 3.0×10^6 the convergence of surface streamlines on the flank of the model reduces and associated open separation is no longer apparent.

- for $Re_l = 4.0 \times 10^6$ the boundary layer on the pressure side near the symmetry plane no longer stays attached until the end of the model as seen at the lower Reynolds numbers.